iScience

CellPress
OPEN ACCESS

Article

WNK1 is required during male pachynema to sustain fertility

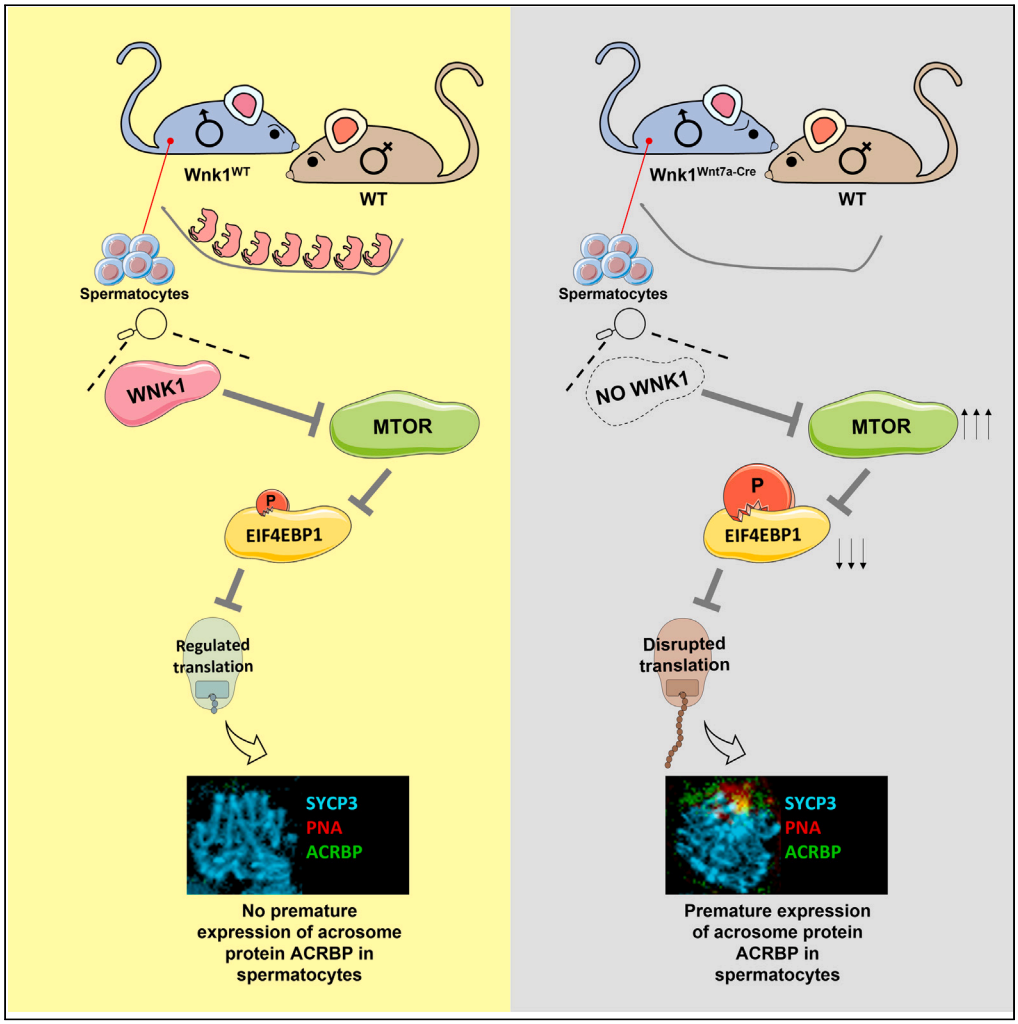

Ru-pin Alicia Chi, Xiaojiang Xu, Jian-Liang Li, ..., Chou-Long Huang, Marcos Morgan, Francesco DeMayo

francesco.demayo@nih.gov

Highlights

The kinase WNK1 is indispensable for spermatogenesis

WNK1 represses MTOR signaling in the spermatocytes

Loss of *Wnk1* is associated with premature expression ACRBP in spermatocytes

Chi et al., iScience *26*, 107616
September 15, 2023
https://doi.org/10.1016/j.isci.2023.107616

iScience

CellPress
OPEN ACCESS

Article

WNK1 is required during male pachynema to sustain fertility

Ru-pin Alicia Chi,[1] Xiaojiang Xu,[2] Jian-Liang Li,[2] Xin Xu,[3] Guang Hu,[3] Paula Brown,[1] Cynthia Willson,[4] Oleksandr Kirsanov,[5] Christopher Geyer,[5,6] Chou-Long Huang,[7] Marcos Morgan,[1] and Francesco DeMayo[1,8,*]

SUMMARY

WNK1 is an important regulator in many physiological functions, yet its role in male reproduction is unexplored. In the male germline, WNK1 is upregulated in preleptotene spermatocytes indicating possible function(s) in spermatogenic meiosis. Indeed, deletion of *Wnk1* in mid-pachytene spermatocytes using the *Wnt7a-Cre* mouse led to male sterility which resembled non-obstructive azoospermia in humans, where germ cells failed to complete spermatogenesis and produced no sperm. Mechanistically, we found elevated MTOR expression and signaling in the *Wnk1*-depleted spermatocytes. As MTOR is a central mediator of translation, we speculated that translation may be accelerated in these spermatocytes. Supporting this, we found the acrosome protein, ACRBP to be prematurely expressed in the spermatocytes with *Wnk1* deletion. Our study uncovered an MTOR-regulating factor in the male germline with potential implications in translation, and future studies will aim to understand how WNK1 regulates MTOR activity and impact translation on a broader spectrum.

INTRODUCTION

Male infertility has been on the rise with a progressive and consistent decline in both semen quality and sperm quantity.[1,2] It has been estimated that 40–50% of the total infertility cases are attributed to male factors,[1] which impacts more than 70 million couples globally.[3] Of particular concern is that a substantial portion of total male fertility cases (estimated to be 30%) remain idiopathic.[4] The lack of identifiable causes poses significant challenges in treatment, leaving those affected without the possibility of conceiving biological children. An improvement in our understanding of factors driving male fertility is thus sorely needed to address this global health issue.

With no lysine (K) kinase 1 (WNK1) is a member of the WNK family of serine/threonine protein kinases. Since its discovery in the early 1990s,[5] WNK1 has been found to regulate numerous cellular processes and is critical in the normal function of multiple organs. In humans, *WNK1* mutation is associated with pseudohypoaldosteronism type II and hereditary sensory and autonomic neuropathy type II,[6,7] leading to an explosion of studies aimed at understanding WNK1's role in the renal and nervous systems. In mouse models, global *Wnk1* deletion causes embryonic lethality prior to E13.5 due to defects in angiogenesis and cardiac development, demonstrating that WNK1 is required for the formation of the cardiovascular system.[8,9] At the cellular level, WNK1 regulates proliferation, migration and differentiation[10]; and subcellularly, WNK1 is known to regulate autophagy,[11] exocytosis,[12] mRNA export,[13] microtubule stability and organization,[14] abscission,[15] and endoplasmic reticulum membrane assembly.[16]

Despite WNK1's pleiotropic functions in the different tissues, its function in the reproductive organs has remained a mystery. We previously identified WNK1 as a regulator of endometrial function downstream of the epidermal growth factor receptor (EGFR),[17] and subsequent *in vitro* analyses suggested WNK1 drives decidualization—an early pregnancy event critical for embryo support and development.[10] These findings were further supported by our recent study using conditional uterine *Wnk1* deletion mice, which resulted in severe subfertility with a spectrum of uterine abnormalities including epithelial hyperplasia, adenomyosis-like features, and impaired embryo implantation.[18]

Adding to the repertoire of growing WNK1 functions, here we report our serendipitous finding that WNK1 is required for spermatogenesis, the stem cell-based developmental process in the testes that produces fertilization-competent sperm. Spermatogenesis begins with spermatogonial stem cells (SSCs), which divide to either self-renew or generate undifferentiated progenitors. These progenitor spermatogonia respond to retinoic acid (RA) to begin a lengthy differentiation program that culminates with their entry into meiosis as preleptotene spermatocytes. Spermatocytes replicate their DNA and progress through meiosis to form haploid round spermatids. Subsequently, round

[1]Reproductive and Developmental Biology Laboratory, National Institute of Environmental Health Sciences, Durham, NC 27709, USA
[2]Integrative Bioinformatics Support Group, National Institute of Environmental Health Sciences, Durham, NC 27709, USA
[3]Epigenetics and Stem Cell Biology Laboratory, National Institute of Environmental Health Sciences, Durham, NC 27709, USA
[4]Integrated Laboratory Systems LLC, Research Triangle Park, NC 27709, USA
[5]Department of Anatomy & Cell Biology at the Brody School of Medicine at East Carolina University, Greenville, NC 27834, USA
[6]East Carolina Diabetes and Obesity Institute, East Carolina University, Greenville, NC 27834, USA
[7]Department of Internal Medicine, University of Iowa Carver College of Medicine, Iowa, IA 52242, USA
[8]Lead contact
*Correspondence: francesco.demayo@nih.gov
https://doi.org/10.1016/j.isci.2023.107616

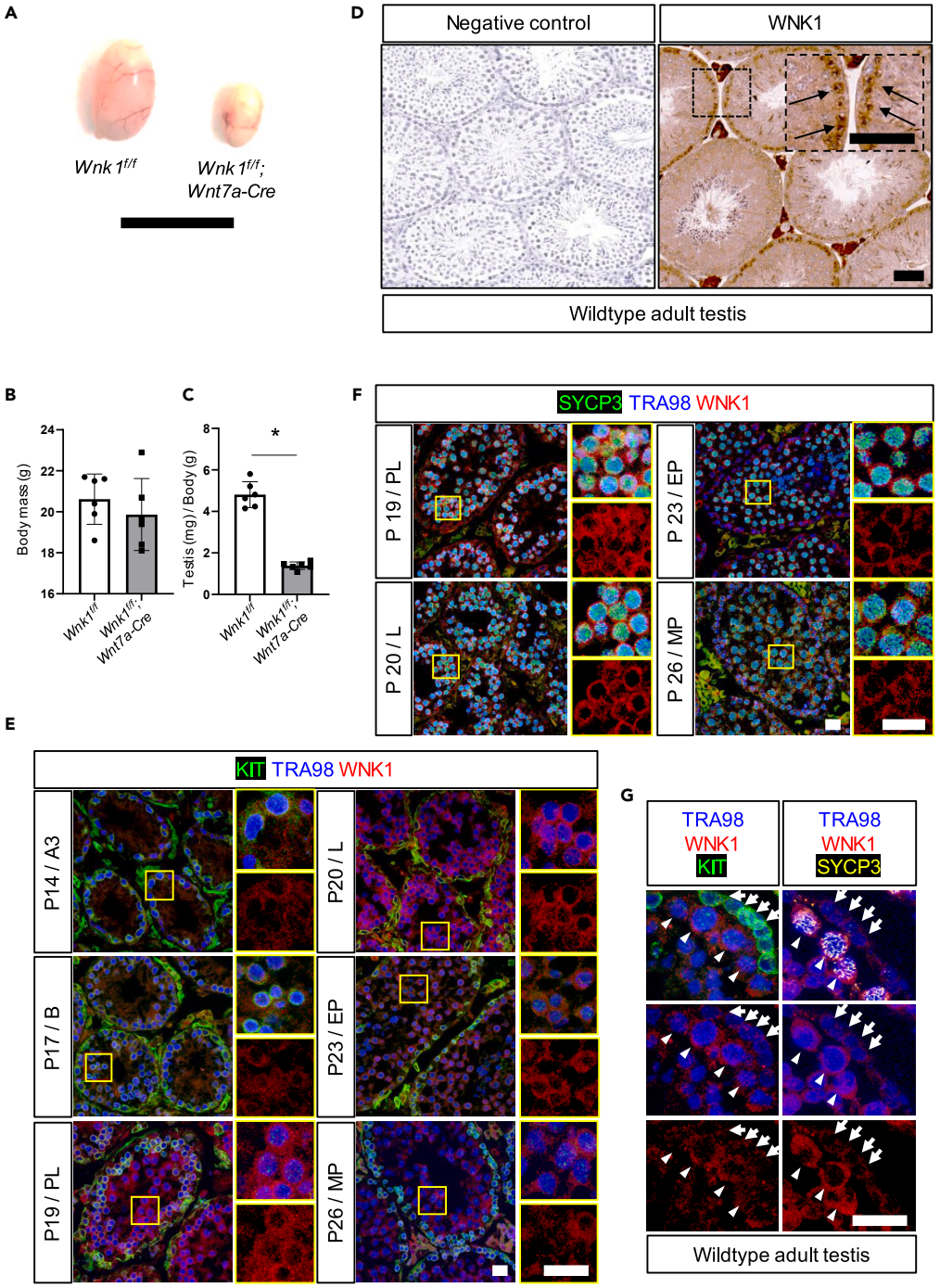

Figure 1. *Wnt7a-Cre* mediated *Wnk1* ablation unexpectedly led to male sterility

(A) Testis from 6–8-week-old *Wnk1*$^{f/f}$ and *Wnk1*$^{f/f}$; *Wnt7a-Cre* male mice, scale bar = 1 cm.

(B and C) Body mass (g) of 6–8-week-old *Wnk1*$^{f/f}$ and *Wnk1*$^{f/f}$; *Wnt7a-Cre* mice (n = 6), and (C). The testis mass (mg) to body mass (g) ratio for 6–8-week-old *Wnk1*$^{f/f}$ and *Wnk1*$^{f/f}$; *Wnt7a-Cre* mice (n = 6). All quantitative results shown are mean ± SD, *p < 0.05, all *t* tests were two-tailed, Student's *t* test for both (B) and (C).

(D) IHC staining in wildtype adult testis to show WNK1 expression. Inset indicates higher WNK1 expression in cells lining the tubule periphery, as indicated by arrows. Negative control = IgG only, scale bars = 50 μm.

(E and F) IF showing WNK1 expression (red) in wild-type mice with synchronized spermatogenesis. P = postnatal day, where mice were treated daily with WIN18,446 from P1 to P10, followed by a single dose of RA on P11. The most advanced cells present at each stage were A3 and B (A_3 and type B spermatogonia) at P14 and P17, respectively; PL, preleptotene spermatocytes at P19, L, leptotene spermatocytes at P20; EP, early pachytene spermatocytes

Figure 1. *Continued*

and MP, mid pachytene spermatocytes at P23 and P26, respectively. KIT or SYCP3 were co-stained in green, and TRA98 was co-stained in blue to mark the germ cells. Scale bar = 20 μm for both magnifications.

(G) IF showing expression of WNK1 (red), KIT (green), SYCP3 (yellow) and TRA98 (blue) in wildtype, 8-week-old mouse testis. *Left panel*: Arrows indicate KIT positive differentiated spermatogonia, and arrowheads show KIT negative spermatocytes. *Right panel*: Arrowheads show SYCP3 positive spermatocytes, while arrows mark SYCP3 negative spermatogonia. Scale bar = 20 μm.

spermatids are remodeled during the morphogenetic program of spermiogenesis to ultimately form testicular sperm. Disturbance to any of these processes can prematurely terminate spermatogenesis or produce non-functional sperm, and both will result in male infertility. The progression through this complex program relies on the expression of genes and proteins in a spatiotemporally controlled manner, which is made possible by precise regulatory mechanisms at each stage. These exist at transcriptional, post-transcriptional and translational levels, and numerous essential factors acting at these different levels have been identified and studied.[19,20]

In this work, we describe an unexpected observation which led to the discovery that WNK1 is crucial for spermatogenesis. We conducted detailed analyses to understand how loss of *Wnk1* impaired spermatogenesis. We show that WNK1 is upregulated as cells transition into meiosis, and that ablation of *Wnk1* during mid-pachynema led to spermatogenic arrest in mid-pachytene spermatocytes which ultimately resulted in azoospermia-associated infertility. Mechanistically, loss of *Wnk1* expression in meiotic spermatocytes elevated MTOR expression and phosphorylation, which in turn activated its downstream substrate, the translation mediator EIF4EBP1. Coincidentally, the post-meiotic acrosome protein ACRBP was prematurely expressed in the *Wnk1*-depleted spermatocytes, demonstrating a possibility that WNK1 may impact translation through MTOR.

RESULTS

Wnt7a-Cre mediated *Wnk1* ablation unexpectedly led to male sterility

In our previous study attempting to understand WNK1's function in the uterus, we used the *Wnt7a-Cre* mouse model to delete *Wnk1* expression with the expectation that *Wnt7a* mediated *Cre* causes gene recombination in the uterine epithelium.[21] An unexpected observation was that the male *Wnk1*$^{f/f}$; *Wnt7a-Cre* offspring were sterile. We first confirmed this by performing breeding trials where the *Wnk1*$^{f/f}$ (control) and *Wnk1*$^{f/f}$; *Wnt7a-Cre* male mice between six and seven weeks of age were housed with wild type females for a period of 6 months during which the female mice were closely monitored for pregnancy and delivery. Within six months, five control males produced a total of 28 litters and 188 pups, while no litters were ever produced from the females housed with the *Wnk1*$^{f/f}$; *Wnt7a-Cre* males. This infertility phenotype revealed that *Wnt7a-Cre* was likely expressed in the males resulting in *Wnk1* deletion which impacted fertility. Gross comparison of *Wnk1*$^{f/f}$ and *Wnk1*$^{f/f}$; *Wnt7a*-Cre mice showed that the primary site affected was the testes (Figure 1A). Besides the infertility and significantly reduced testis weights, the *Wnk1*$^{f/f}$ and *Wnk1*$^{f/f}$; *Wnt7a*-Cre mice appeared otherwise indistinguishable in terms of behavior, body mass (Figure 1B), and gross morphology of other organs. The testis-to-body mass ratios of the *Wnk1*$^{f/f}$; *Wnt7a*-Cre mice were only ~30% of their *Wnk1*$^{f/f}$ littermates (Figure 1C), suggesting that infertility was possibly due to impaired spermatogenesis and loss of advanced germ cells.

Wnk1 is upregulated during the spermatogonia to spermatocyte transition

Although *Wnk1* mRNA and protein levels were previously reported in whole testes,[22,23] its expression trend and regulation in specific somatic or germ cell types remain unknown. Therefore, we first examined WNK1 protein expression during steady-state spermatogenesis in the testes of adult wild-type mice by immunohistochemistry (IHC). WNK1 was expressed in all intratubular cells and not confined to any stage of the spermatogenic progression (Figure 1D), and a closer examination revealed that in some tubules, cells closer to the basement membrane had the highest WNK1 protein levels (Figure 1D, inset, arrows). To define the specific cells expressing high WNK1 levels, we next synchronized spermatogenesis in the developing testis to obtain defined germ cell types at different stages of development.[24,25] Briefly, mice were orally dosed with the potent and selective RA synthesis inhibitor WIN 18,446 daily from postnatal day 1 (P1) to P10, which prevented spermatogonial differentiation. As a result, progenitor spermatogonia proliferated without differentiating and entering meiosis. On P11, a single dose of RA was administered, and progenitor spermatogonia differentiated synchronously. Owing to the precise timing of each spermatogenic stage, the cell populations present in the testis at different time points post RA stimulation can be accurately determined.[24] Mice were euthanized at the following ages, and the most advanced germ cells are indicated in parentheses: P14 (type A_3 spermatogonia), P17 (type B spermatogonia), P19 (preleptotene spermatocytes), P20 (leptotene spermatocytes), P23 (early pachytene spermatocytes), and P26 (mid-pachytene spermatocytes). WNK1 expression was determined by immunofluorescence (IF), and the pan germ cell marker TRA98, the differentiating spermatogonia marker KIT, and the spermatocyte marker SYCP3 were co-immunostained to define the germ cell differentiation stage. Successful synchronization was confirmed by the presence of KIT-positive differentiating spermatogonia at P14 and P17 (Figure 1E), and the presence of SYCP3-positive foci on P19 as expected for preleptotene spermatocytes (Figure 1F). While WNK1 is detectable in differentiating spermatogonia, its levels increased significantly at the preleptonema stage (Figure 1E). WNK1 levels remained high during leptonema and early pachynema, and thereafter, WNK1 levels decreased slightly as the cells reached mid-pachynema but remained higher than pre-meiotic levels (Figures 1E and 1F). These results indicated that WNK1 was expressed throughout early spermatogenesis, with an upregulation during the spermatogonia to spermatocyte transition, resulting in high expression in spermatocytes starting at the preleptonema/leptonema stage.

To ensure that WNK1 expression followed a similar trend in steady-state spermatogenesis, we next examined testes from post-pubertal wild-type mice. WNK1 was immunolabeled in conjunction with KIT or SYCP3 to differentiate between the spermatogonia and spermatocyte

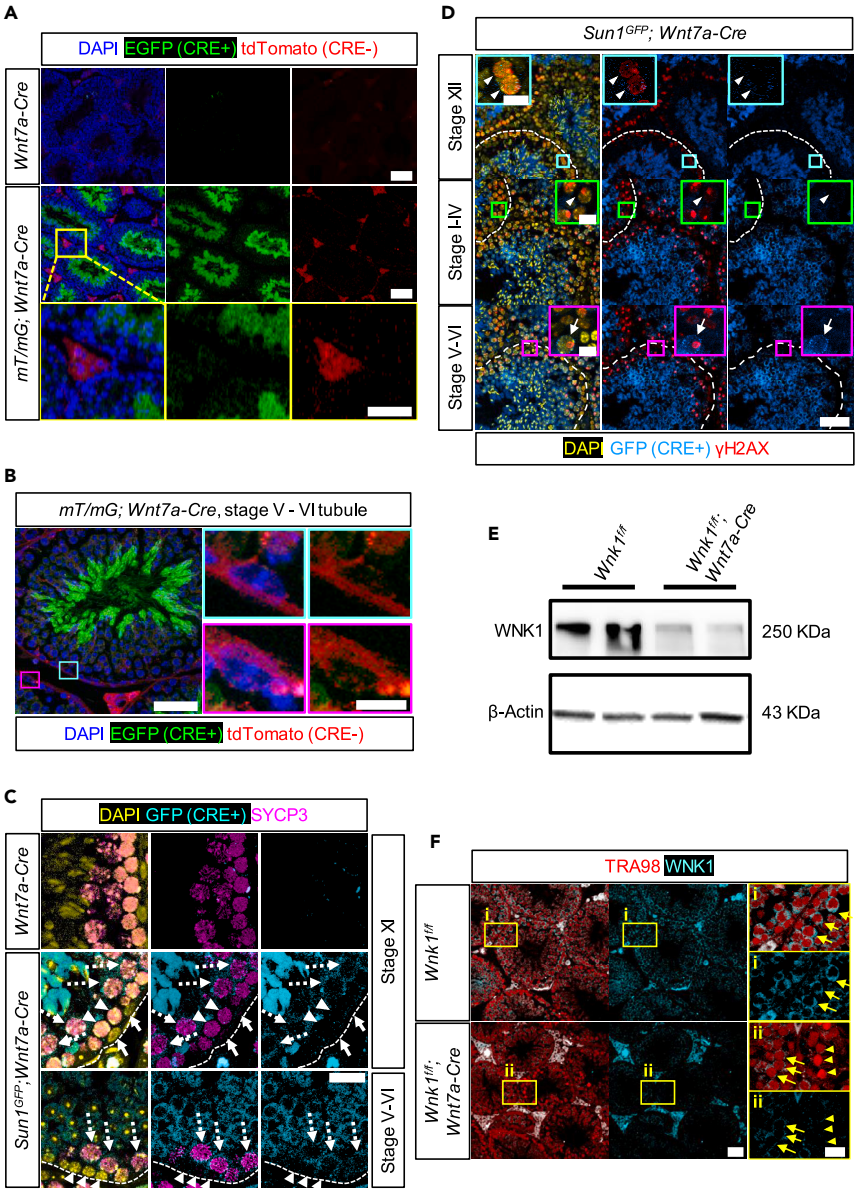

Figure 2. Detection of recombined *loxP* alleles in the germline of *Wnt7a-Cre* mice

(A) Endogenous EGFP (green) and tdTomato (red) expression from testis of the control (*Wnt7a*-Cre) mice and the reporter (*mT/mG*; *Wnt7a-Cre*) mice, which expressed EGFP in *Wnt7a-Cre*-positive cells; and tdTomato in *Wnt7a-Cre*-negative cells. Nuclei were counterstained with DAPI and shown in blue, scale bars = 100 μm for top and middle panels, and 50 μm for the bottom panel.

(B) Endogenous EGFP (green) and tdTomato (red) expression in a stage V–VI tubule from the *mT/mG*; *Wnt7a-Cre* mouse. Insets show two independent Sertoli cells, and DAPI stain show nuclei in blue, scale bars = 50 μm (large image) and 10 μm (insets).

(C) GFP (cyan) and SYCP3 (purple) immunostaining of testicular cross sections from the *Wnt7a-Cre* control mice, and the *Sun1*^{GFP}; *Wnt7a-Cre* reporter mice, which expresses nuclear-membrane localized GFP in *Wnt7a-Cre*-positive cells. Stage XI tubules are shown in the top and middle panels, and stage V–VI tubule is shown in the bottom panel. Dashed white lines denote tubule boundary, and DAPI shows nuclei in yellow. *Top panel*: Negative control showing testis cross section from the *Wnt7a-Cre* mice subjected to immunolabeling of GFP (cyan) and SYCP3 (purple). *Middle panel*: Dashed arrows mark GFP-positive and SYCP3-positive diplotene spermatocytes, arrowheads indicate GFP-negative and SYCP3-positive zygotene spermatocytes, and arrows show GFP-negative, SYCP3-negative spermatogonia. *Bottom panel*: dashed arrows show GFP-positive, SYCP3-positive pachytene spermatocytes and arrowheads mark GFP-negative and SYCP-negative B spermatogonia. Scale bar = 20 μm.

(D) GFP (blue) and γH2AX (red) immunostaining of testis cross sections from *Sun1*^{GFP}; *Wnt7a-Cre* mice. Nuclei are shown by DAPI in yellow and dashed white lines outline the tubule of interest with its stage annotated on the left. Insets show zygotene spermatocytes from stage XII tubule, and pachytene spermatocytes from the rest. Arrowheads show GFP-negative cells, and arrows indicate GFP-positive cells. Note that the middle and bottom panels are showing different tubules from the same image. Scale bars = 50 μm for large images, and 10 μm for the insets.

Figure 2. *Continued*

(E) Western blot showing WNK1 protein levels in the whole-testis from *Wnk1*$^{f/f}$ and *Wnk1*$^{f/f}$; *Wnt7a-Cre* mice, β-Actin serves as loading control.

(F) WNK1 (cyan) and TRA98 (red) immunostaining of testis cross sections from adult *Wnk1*$^{f/f}$ and *Wnk1*$^{f/f}$; *Wnt7a-Cre* mice. Arrows show meiotic cells, and arrowheads indicate some germ cells without WNK1 expression. Scale bars = 50 μm for large images, and 20 μm for the insets.

populations (Figure 1G). WNK1 expression is visibly higher in KIT-negative spermatocytes as compared to neighboring KIT-positive differentiating spermatogonia (Figure 1G, left panel). Similarly, SYCP3-positive spermatocytes exhibited higher WNK1 levels in comparison to adjacent SYCP3-negative spermatogonia (Figure 1G, right panel). To further confirm these results, we also analyzed WNK1 expression in tubules of different stages by co-immunolabeling with peanut agglutinin (PNA), a lectin which binds to the acrosome membrane and displays unique patterns at the different stages of the seminiferous cycle.[26] Comparison of neighboring stage VI and stage VIII tubules revealed an increase of WNK1 expression from B spermatogonia (Figure S1, stage VI, SYCP3-negative cells indicated by arrows) to preleptotene spermatocytes (Figure S1, stage VIII, SYCP3-positive cells indicated by arrowheads), confirming that in adult steady-state spermatogenesis, WNK1 expression is induced as cells enter the meiotic phase. Next, we examined whether WNK1 levels decrease during the pachynema phase as observed in synchronized spermatogenesis. Here, we compared neighboring tubules at stages II and VI representing early pachytene and mid-pachytene spermatocytes (Figure S2). We found that WNK1 levels decreased in stage VI SYCP3-positive spermatocytes compared to stage II SYCP3-positive spermatocytes (Figure S2, arrowheads mark the spermatocyte population). Lastly, we also examined a stage X tubule where late-pachytene spermatocytes line the zygotene spermatocytes (Figure S3). Indeed, WNK1 expression was visibly higher in the zygotene spermatocytes (Figure S3, arrowheads) compared to late-pachytene spermatocytes (Figure S3, arrows). Taken together, we demonstrate that WNK1 exhibited similar expression pattern in synchronized and steady-state spermatogenesis, which peaks during preleptonema/leptonema, and decreases during pachynema progression.

Detection of recombined *loxP* alleles in mid-pachytene spermatocytes of *Wnt7a-Cre* mice

Based on WNK1's testicular expression in wild-type mice and the substantial reduction of testis size in the *Wnk1*$^{f/f}$; *Wnt7a-Cre* mice, we speculated that *Wnt7a-Cre* was expressed in the testis. To test this, we examined the localization of the *Cre* activity in the testes of *mT/mG*; *Wnt7a-Cre* reporter mice.[27] These mice express membrane-targeted tdTomato (mT) in *Cre*-negative cells, and membrane-targeted EGFP (mG) in *Cre*-positive cells. EGFP was detected only in the intratubular space while all interstitial cells were tdTomato-positive (Figure 2A). This indicated that *Wnt7a* is not expressed in the Leydig cells. In addition, closer examination within the tubules indicated that Sertoli cells were also tdTomato-positive and EGFP-negative (Figure 2B, insets). Hence, the sterility phenotype observed in the *Wnk1*$^{f/f}$; *Wnt7a-Cre* mice was not associated with *Wnk1* depletion in Sertoli or Leydig cells. EGFP expression was evidently in the germ lineage, and while EGFP accumulation became apparent in round and especially elongating spermatids, expression in the spermatocytes appeared ambiguous (Figures 2A and 2B). To further assess this, we next examined SYCP3 and CRE (EGFP) in parallel by immunolabeling (Figures 2C and 2D). Here, to accurately define the nuclear boundary, we further generated the *Sun1*^{GFP}; *Wnt7a-Cre* reporter mice, in which EGFP is specifically localized to the nuclear membrane of *Cre*-positive cells.[28] To enhance the GFP signal, we immunolabeled GFP using a GFP specific antibody, and the specificity of the GFP antibody was confirmed as no GFP was observed in the *Wnt7a-Cre* control mice (Figure 2C, top panel). No CRE activity (lack of EGFP) was detected in SYCP3-negative spermatogonia (Figure 2C, solid arrows in middle panel). In addition, SYCP3-negative B cells and SYCP3-positive zygotene spermatocytes were both EGFP-negative (Figure 2C, arrowheads in bottom panel and arrowheads in middle panel, respectively), suggesting that *Wnt7a* is not expressed at these stages. EGFP was detected in the pachytene and diplotene spermatocytes (Figure 2C, dashed arrows in the bottom and top panels, respectively). This indicated that EGFP expression was likely first present in pachytene spermatocytes. To further pinpoint the onset of *Wnt7a-Cre* activity, we co-immunolabeled phosphorylated H2AX (γH2AX) which exhibits distinctive expression trends during prophase of meiosis I (Figure S4).[29] Here, no EGFP was observed in zygotene spermatocytes in stage XII tubule, confirming that EGFP was not expressed throughout zygonema (Figure 2D, top panel). EGFP was still not detected in early stage pachytene spermatocytes, indicating that CRE activity likely initiated after pachynema onset (Figure 2D, middle panel). EGFP became visible around the nuclear membrane during stage V–VI (Figure 2D, bottom panel), suggesting that the onset of *Wnt7a*-mediated CRE activity is likely during mid-pachynema in the primary spermatocytes. Next, to confirm that *Wnt7a-Cre* is inducing *Wnk1* deletion in the male germline in the *Wnk1*$^{f/f}$; *Wnt7a-Cre* mice, WNK1 protein levels were assayed by western blot and IF. Whole testis lysates contained markedly lower WNK1 levels in the *Wnk1*$^{f/f}$; *Wnt7a-Cre* mice compared to littermate controls (Figure 2E), confirming CRE-induced gene recombination and thus *Wnk1* deletion in the testis. WNK1 immunolabeling using testis cross sections also supported this, where WNK1 was readily detected in the *Wnk1*$^{f/f}$ testis which was higher in meiotic cells (Figure 2F inset i, arrows). In the *Wnk1*$^{f/f}$; *Wnt7a-Cre* mice, the level of WNK1 in spermatocytes are markedly lower compared to the *Wnk1*$^{f/f}$ spermatocytes (Figure 2F inset ii, arrows). Cells further down the differentiation pathway showed no detectable WNK1 expression (Figure 2F inset ii, arrowheads indicate few such cells), confirming WNK1 deletion after CRE activation in the *Wnk1*$^{f/f}$; *Wnt7a-Cre* mice.

Since the male germline expression of the *Wnt7a-Cre* and WNK1's critical function during spermatogenesis are both new findings, we first confirmed the phenotype using a second germline *Cre*, *Hspa2-Cre* which is activated in leptotene/zygotene spermatocytes.[30] *Wnk1*$^{f/f}$; *Hspa2-Cre* mice exhibited infertility and reduced testicular sizes (Figure S5), providing further support that *Wnk1* deletion in the spermatocytes caused male infertility. Lastly, given that *Wnt7a* is not exclusively expressed in the male germline, we further confirmed that it was the deletion of *Wnk1* from the germline that caused infertility in the *Wnk1*$^{f/f}$; *Wnt7a-Cre* mice, and not loss of *Wnk1* in other organs. To address this, we used the tamoxifen (TAM)-inducible *Ddx4-Cre*^{ERT} mouse model, which drives *Wnk1* deletion only in the germline upon TAM treatment.[31] CRE activity and *Wnk1* deletion were first confirmed by western blot of testicular lysates, which showed substantial WNK1 reduction in

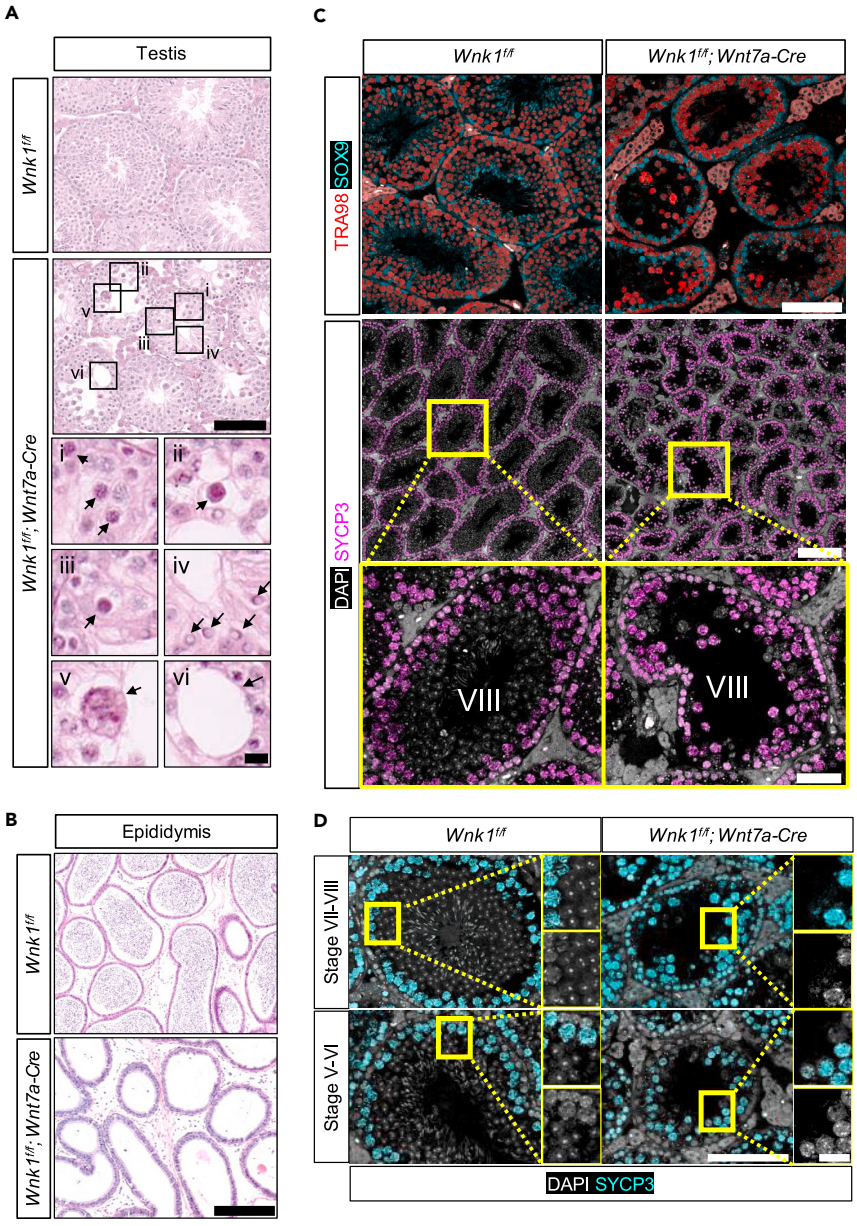

(figure continued on next page)

TAM-treated *Wnk1*$^{f/f}$; *Ddx4-Cre*^{ERT2} mice, as compared to TAM-treated *Wnk1*$^{f/f}$ littermate controls (Figure S6). Indeed, the *Wnk1*$^{f/f}$; *Ddx4-Cre*^{ERT2} mice were infertile with smaller testes (Figure S6), confirming that it is the germline-specific deletion of *Wnk1*, and not other *Wnt7a*-expressing cells that caused infertility in the *Wnk1*$^{f/f}$; *Wnt7a-Cre* mice.

Loss of *Wnk1* caused meiotic arrest during mid-pachynema

The *Wnk1*$^{f/f}$; *Wnt7a-Cre* mice exhibited severely disrupted spermatogenesis as indicated by histology (Figure 3A). The constituting tubules were decreased in diameter owing to the decreased number of germ cells which lead to disorganization and thinness of germinal epithelium. Germ cell degeneration was observed in a variety of ways, including spermatocytes with hypereosinophilic, contracted cytoplasm and pyknotic nuclei indicative of apoptosis (Figure 3A, i–iii). The round spermatids were rare and those that were present appeared morphologically abnormal with ring forms and marginated chromatin (Figure 3A, iv). Further, multinucleated giant cells which indicates aggregation and degeneration of the round spermatids were also observed (Figure 3A, v). Vacuolation of the Sertoli cells further indicated generalized germinal cell

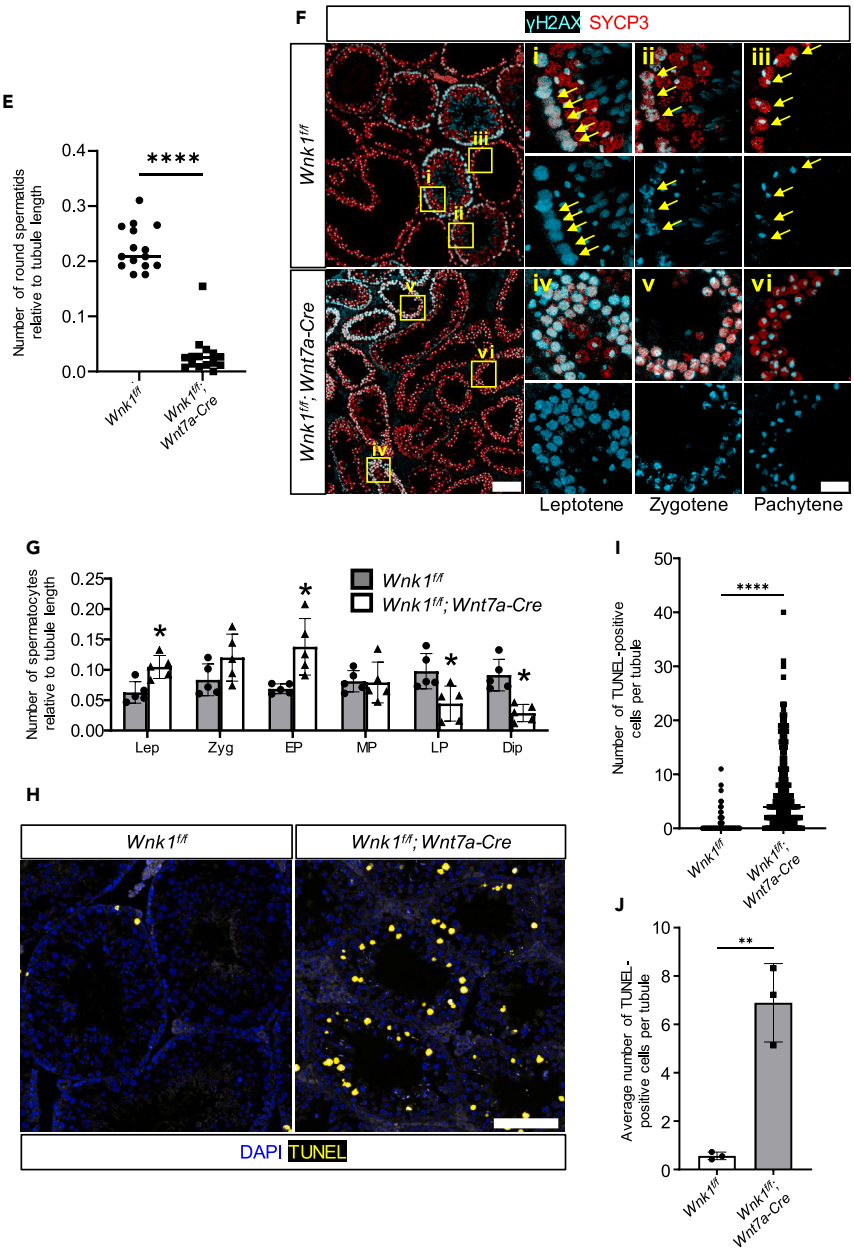

Figure 3. Loss of *Wnk1* causes meiotic arrest during mid-pachynema

(A) Hematoxylin and eosin (H and E) staining of testicular cross sections from the *Wnk1*$^{f/f}$ and *Wnk1*$^{f/f}$; *Wnt7a-Cre* mice. Insets show pyknotic nuclei (i–iii), rare round spermatids with ring forms and marginated chromatins (iv), multinucleated giant cell (v), and vacuolation of Sertoli cells (vi). Scale bar = 100 μm for large images, and 10 μm for insets.

(B) H and E staining of the cauda epididymis from the *Wnk1*$^{f/f}$ and *Wnk1*$^{f/f}$; *Wnt7a-Cre* mice. Scale bar = 200 μm.

(C) *Top panel:* Dual immunolabeling of TRA98 (red) and SOX9 (cyan) of testis cross sections from the *Wnk1*$^{f/f}$ and *Wnk1*$^{f/f}$; *Wnt7a-Cre* mice to show the germ and somatic populations, respectively. Scale bar = 100 μm. *Middle and bottom panels*: SYCP3 immunostaining of testis cross sections to show meiotic cells in the *Wnk1*$^{f/f}$ and *Wnk1*$^{f/f}$; *Wnt7a-Cre* mice. Insets (bottom panel) show magnification of a stage VIII tubule, and nuclei is marked by DAPI in white. Scale bars = 200 μm (middle panel) and 50 μm (bottom panel).

(D) SYCP3 (cyan) immunostaining to show SYCP3-negative post-meiotic cells in the testis of *Wnk1*$^{f/f}$ and *Wnk1*$^{f/f}$; *Wnt7a-Cre* mice. Insets show magnification of stage VII–VIII and V–VI tubules (top and bottom panels, respectively), and nuclei is marked by DAPI in white. Scale bar = 100 μm for the larger image, and 20 μm for the insets.

(E) Quantification of round spermatids in stage I–VIII tubules from the *Wnk1*$^{f/f}$ and *Wnk1*$^{f/f}$; *Wnt7a-Cre* mice. The number of spermatids were normalized to tubular length, and 15 tubules were counted from three independent mice for each group. ****p < 0.0001 based on the Mann-Whitney U test.

Figure 3. *Continued*

(F) γH2AX (cyan) and SYCP3 (red) dual immunostaining of the *Wnk1*$^{f/f}$ and *Wnk1*$^{f/f}$; *Wnt7a-Cre* testes to identify leptotene (insets i and iv, arrows), zygotene (insets ii and v, arrows) and pachytene spermatocytes (insets iii and vi, arrows). Scale bar = 100 μm for large images and 20 μm for insets.

(G) Quantification of the number of leptotene (Lep), zygotene (Zyg), early pachytene (EP, stages I–IV), mid-pachytene (MP, stages V–VIII) and late pachytene (LP, stages IX –X), and diplotene spermatocytes (Dip, stage XI) in the tubules of the *Wnk1*$^{f/f}$ and *Wnk1*$^{f/f}$; *Wnt7a-Cre* mice, normalized to the tubule length. Five tubules from three independent mice were quantified, results shown are mean ± SD, *p < 0.05 based on two-tailed Student's *t* test.

(H) TUNEL (yellow) IF staining of the testes from control and *Wnk1*$^{f/f}$; *Wnt7a-Cre* testes to show apoptotic cells. Nuclei were counterstained with DAPI (blue), and scale bar = 100 μm.

(I) Number of TUNEL-positive cells per tubules in 128 and 215 tubules from three *Wnk1*$^{f/f}$ and three *Wnk1*$^{f/f}$; *Wnt7a-Cre* mice, respectively. Each dot represents one tubule, and line indicates median. ****p < 0.0001 based on the Mann-Whitney U test.

(J) The average number of TUNEL-positive cells per tubule for the three individual *Wnk1*$^{f/f}$ and *Wnk1*$^{f/f}$; *Wnt7a-Cre* mice. Results shown are mean ± SD, **p < 0.0005 based on two-tailed Student's *t* test.

degeneration or atrophy (Figure 3A, vi). Elongated spermatids were not observed in any of the *Wnk1*$^{f/f}$; *Wnt7a-Cre* testes suggesting spermatogenic arrest prior to formation of elongated spermatids. This was confirmed by the absence of sperm in the epididymis (Figure 3B).

Next, we examined germ and somatic populations using TRA98 and SOX9 immunolabeling in the control and *Wnk1*$^{f/f}$; *Wnt7a-Cre* testes. Evidently, *Wnk1*$^{f/f}$; *Wnt7a-Cre* testes contained substantially less TRA98-positive cells (Figure 3C, top), confirming the loss of germ lineage in the *Wnk1*$^{f/f}$; *Wnt7a-Cre* mice. In addition, all tubules in the *Wnk1*$^{f/f}$; *Wnt7a-Cre* testes contained SYCP3-positive cells, indicating that meiotic initiation was likely not impeded (Figure 3C, middle and bottom panels). A closer examination revealed that in the *Wnk1*$^{f/f}$ control testis, all stage I–VIII tubules contained round spermatids (Figure 3D, left panel). However, in the *Wnk1*$^{f/f}$; *Wnt7a-Cre* testis, the number of round spermatids in stage I–VIII tubules were either rare or absent (Figure 3D, right panel), indicating that the arrest occurred prior to meiotic completion. This was confirmed by quantitative analyses where the number of round spermatids in stage I–VIII tubules were counted and normalized to the tubule length (Figure 3E). We next analyzed the spermatocyte populations to determine whether spermatogenesis was arrested at the meiotic stage. Here, we dual labeled the cells with γH2AX and SYCP3 to define the meiotic stage of the primary spermatocytes. Combined with staging of the tubules, cells labeled with γH2AX and SYCP3 were categorized into leptotene, zygotene, and pachytene spermatocytes in control testes (Figure 3F, top half). While the same spermatocyte populations were present in the *Wnk1*$^{f/f}$; *Wnt7a-Cre* testes, they appeared to be in altered quantities compared to control testes (Figure 3F, bottom half). We next quantified the number of leptotene spermatocytes (stages IX–X), zygotene spermatocytes (stages XI–XII), early pachytene spermatocytes (stages I–IV), mid-pachytene spermatocytes (stages V–VIII), late-pachytene spermatocytes (stages IX–X), and diplotene spermatocytes (stage XI) in the *Wnk1*$^{f/f}$ *and Wnk1*$^{f/f}$; *Wnt7a-Cre* testes. This revealed that at the leptonema, zygonema, and early pachynema stages, more spermatocytes were present in the *Wnk1*$^{f/f}$; *Wnt7a-Cre* mice compared to the *Wnk1*$^{f/f}$ mice (Figure 3G). Spermatocyte numbers were comparable during mid-pachynema but by late-pachynema, the *Wnk1*$^{f/f}$; *Wnt7a-Cre* mice had significantly fewer spermatocytes compared to the *Wnk1*$^{f/f}$ mice (Figure 3G). The ratio of early-: mid-: late-pachytene spermatocytes was 1: 1.181: 1.422 in the *Wnk1*$^{f/f}$ mice, whereas in the *Wnk1*$^{f/f}$; *Wnt7a-Cre* mice, the ratio was 1: 0.602: 0.366. This suggested that the primary arrest occurred during mid-pachynema, which was also the stage during which *Wnt7a* expression initiated. As failure of meiosis triggers apoptosis, we next examined apoptotic activities via TUNEL assay (Figure 3H). We quantified apoptosis by counting the TUNEL-positive cells in 128 and 215 tubule cross sections from three *Wnk1*$^{f/f}$ and three *Wnk1*$^{f/f}$; *Wnt7a-Cre* testes, respectively (Figure 3I), which revealed a significant increase of apoptosis in the *Wnk1*$^{f/f}$; *Wnt7a-Cre* testes. The average number of TUNEL-positive cells per tubule was 0.56 ± 0.16 and 6.89 ± 1.62 for the control and *Wnk1*$^{f/f}$; *Wnt7a-Cre* mice, respectively (Figure 3J). Together, these findings confirmed that WNK1 deletion from mid-pachytene spermatocytes led to spermatogenic arrest during mid-pachynema which was associated with increased apoptosis.[32]

Single-cell RNA-seq (scRNA-seq) confirmed meiotic impairment in the *Wnk1*$^{f/f}$; *Wnt7a-Cre* testes

To characterize the impact of *Wnk1* deletion on meiosis at the molecular level, we profiled the transcriptomes of the *Wnk1*$^{f/f}$ and *Wnk1*$^{f/f}$; *Wnt7a-Cre* germ cells. Testicular single-cell suspensions were obtained from *Wnk1*$^{f/f}$ and *Wnk1*$^{f/f}$; *Wnt7a-Cre* mice aged between six and eight weeks. Cells were then processed by the 10X Genomics Chromium Controller to create single-cell libraries for sequencing. In total, 12,656 and 13,437 cells were captured and sequenced from the *Wnk1*$^{f/f}$ and *Wnk1*$^{f/f}$; *Wnt7a-Cre* testes, respectively. Of these, 9,436 and 9,833 cells from the respective mice passed standard quality control and were retained for subsequent analyses. On average, 21,019 unique molecular indices (UMIs) and 3,976 genes were detected per cell from the *Wnk1*$^{f/f}$ testes, and 15,836 UMIs and 4,132 genes per cell were detected from the *Wnk1*$^{f/f}$; *Wnt7a-Cre* testes. Unsupervised clustering identified major cell types belonging to both germ and somatic lineages (Figure 4A). Based on marker gene expression, somatic cells were identified including Sertoli, Leydig, and macrophages (Figure S7). Germ cells were subdivided, based on expression of established markers,[33] into distinct populations that included subtypes of spermatogonia (stem, progenitor, and differentiating), meiotic spermatocytes, and post-meiotic spermatids (Figure 4B). Note that in mouse spermatogenesis, *Stra8* is expressed in progenitor to A_2 differentiated spermatogonia and preleptotene spermatocytes, but then reduced in leptotene and zygotene spermatocytes.[33] Based on the marker gene expression, the clusters were accordingly annotated: SSC = spermatogonial stem cells; pSPG = progenitor spermatogonia; dSPG = differentiating spermatogonia; SPC1–SPC4 = spermatocytes; and SPT1–SPT4 = spermatids (Figure 4C). These annotations were confirmed by trajectory modeling using Monocle,[34] in which pseudotime values were assigned to each cell, revealing a developmental progression starting at the SSC, followed by pSPG and dSPG, then SPC1–4 and finally, SPT1–4 in the *Wnk1*$^{f/f}$ and *Wnk1*$^{f/f}$; *Wnt7a-Cre* testes (Figure 4D). *Wnt7a* is detected mostly in the SPC3 cluster, suggesting that this cluster consists of mid-pachytene

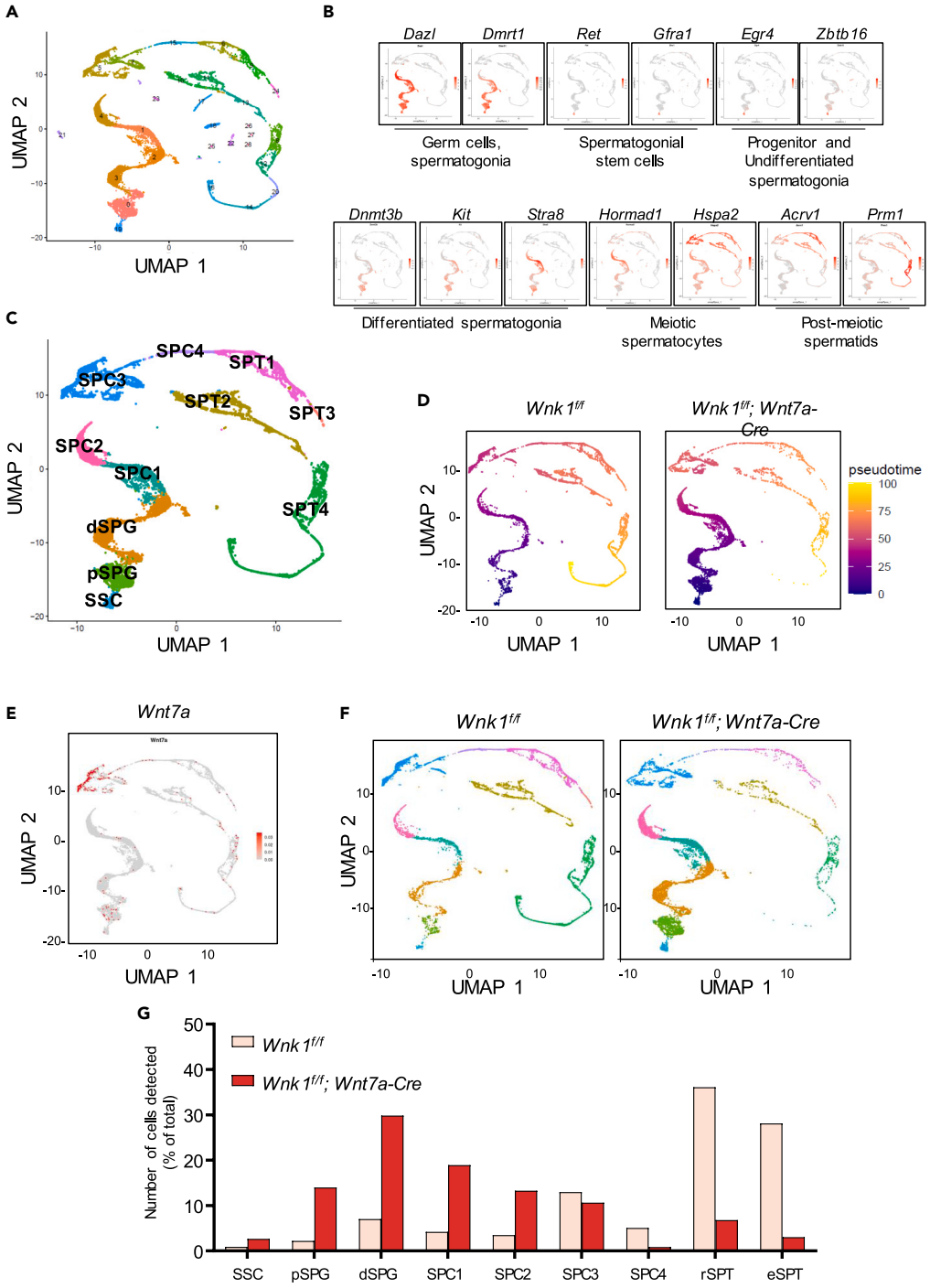

(figure continued on next page)

spermatocytes (Figure 4E). The cell populations in the *Wnk1*$^{f/f}$ and *Wnk1*$^{f/f}$; *Wnt7a-Cre* testes were markedly different—while *Wnk1*$^{f/f}$ control testes possessed cells throughout the entire spermatogenic program from SSCs to elongating spermatids, the *Wnk1*$^{f/f}$; *Wnt7a-Cre* testes contained high numbers of spermatogonia and early to mid-stage spermatocytes with few late-stage spermatocytes or spermatids (Figure 4F). Examination of the number of cells in each cluster (as a % to the total number of cells) further revealed that the arrest occurred around the SPC3 stage, as the SPC3 to SPC2 ratio for *Wnk1*$^{f/f}$; *Wnt7a-Cre* mice were drastically lower than *Wnk1*$^{f/f}$ controls (0.80 vs. 3.73, Figure 4G).

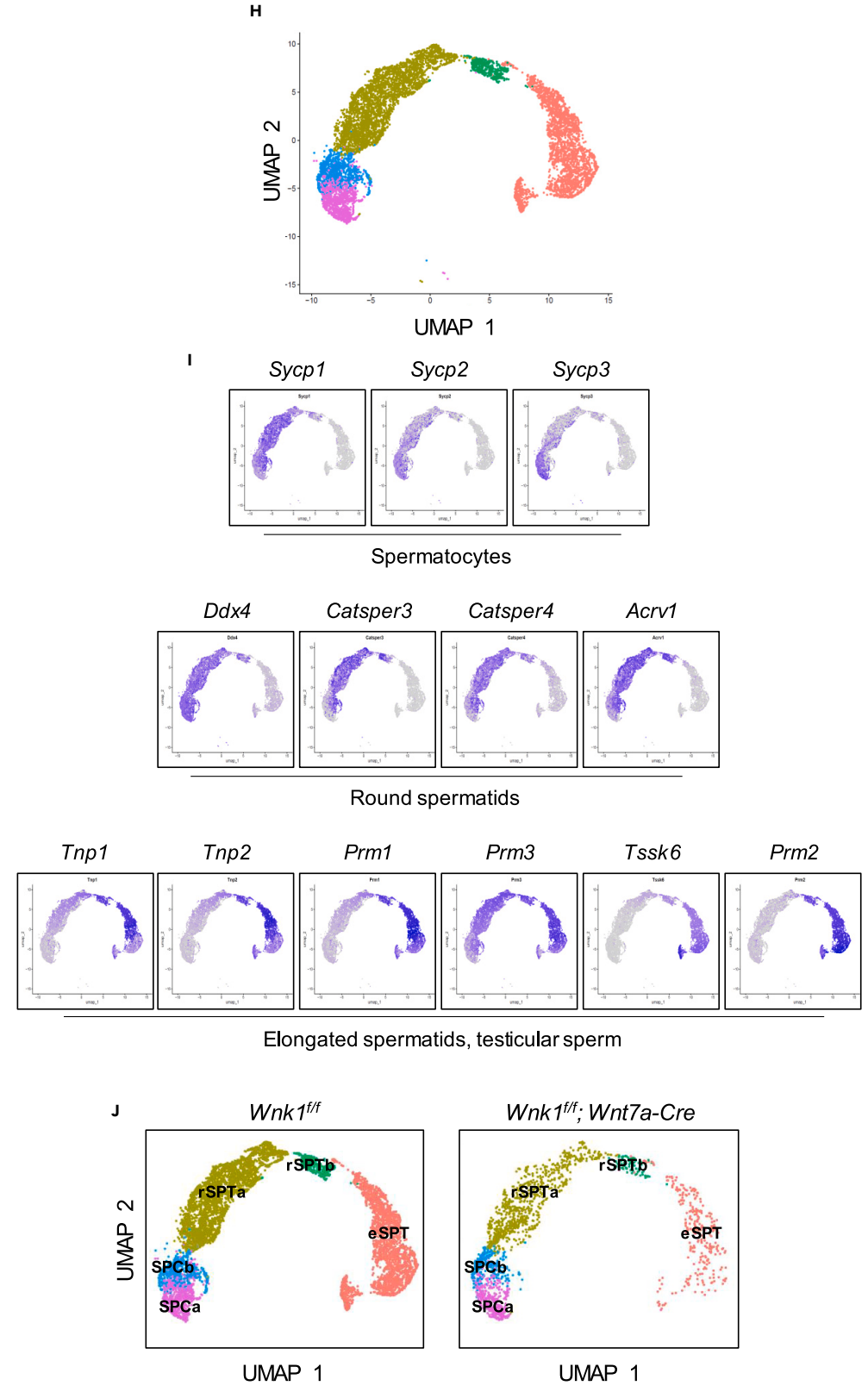
H
UMAP 2
UMAP 1
I
Sycp1
Sycp2
Sycp3
Spermatocytes
Ddx4
Catsper3
Catsper4
Acrv1
Round spermatids
Tnp1
Tnp2
Prm1
Prm3
Tssk6
Prm2
Elongated spermatids, testicular sperm
J
Wnk1f/f
Wnk1f/f; Wnt7a-Cre
rSPTb
rSPTa
eSPT
SPCb
SPCa
UMAP 2
UMAP 1
UMAP 1

Figure 4. Single-cell RNA-seq (scRNA-seq) confirmed meiotic impairment in the *Wnk1*$^{f/f}$; *Wnt7a-Cre* testes

(A) UMAP clustering of the combined testicular cells from three *Wnk1*$^{f/f}$ and two *Wnk1*$^{f/f}$; *Wnt7a-Cre* mice, which identified 28 clusters.

(B) Expression patterns of selected spermatogonial, meiotic and post-meiotic marker genes corresponding to each cellular state on the UMAP plots: *Dazl* and *Dmrt1* (germ cells); *Ret*, and *Gfra1* (spermatogonial stem cells); *Egr4* and *Zbtb16*/*Plzf* (undifferentiated progenitor spermatogonia); *Dnmt3b*, *Kit* and *Stra8** (differentiated spermatogonia); *Hormad1* and *Hspa2* (meiotic spermatocytes); as well as *Acrv1* and *Prm1* (post-meiotic spermatids). *Note that in mice, *Stra8* expression is detected in differentiated spermatogonia as well as preleptotene to zygotene spermatocytes.[33]

(C) Annotation of each germline UMAP cluster based on marker gene expression: SSC = spermatogonial stem cells; pSPG and dSPG = progenitor and differentiated spermatogonia, respectively; SPC1 – SPC4 = spermatocytes; and SPT1 – SPT4 = spermatids.

(D) Pseudotime reconstruction of the germ cell developmental trajectory starting at the SSC cluster and ending in the SPT4 cluster in the *Wnk1*$^{f/f}$ and *Wnk1*$^{f/f}$; *Wnt7a-Cre* testes.

(E) Onset of *Wnt7a* expression in SPC3 cluster, indicating CRE activation and *Wnk1* deletion.

(F) UMAP clustering of the *Wnk1*$^{f/f}$ (left) and *Wnk1*$^{f/f}$; *Wnt7a-Cre* (right) germ lineage through the spermatogenic progression.

(G) The number of cells present at each spermatogenic stage in the *Wnk1*$^{f/f}$ and *Wnk1*$^{f/f}$; *Wnt7a-Cre* testes, expressed as % of total cells in the respective libraries.

(H) UMAP clustering of the germ cells with *Wnk1* deletion (i.e., clusters SPC3, SPC4, SPT1, SPT2, SPT3, and SPT4 from C) identified five clusters.

(I) Expression patterns of selected meiotic, round spermatids and elongated spermatids marker genes corresponding to each cellular state on the UMAP plots: *Sycp1*, *Sycp2* and *Sycp3* (spermatocytes); *Ddx4*, *Catsper3*, *Catsper4* and *Acrv1* (round spermatids); and *Tnp1*, *Tnp2*, *Prm1*, *Prm3*, *Tssk6* and *Prm2* (elongated spermatids and testicular sperm). Note that *Ddx4* expression decreases in elongated spermatids.

(J) Annotation of each UMAP cluster based on marker gene expression for the *Wnk1*$^{f/f}$ testes and the *Wnk1*$^{f/f}$; *Wnt7a-Cre* testes: SPCa and SPCb = spermatocytes encompassing mid-pachytene spermatocytes to secondary spermatocytes; rSPTa and rSPTb, round spermatids; eSPT elongated spermatids and testicular sperm.

This finding supports our histological observations that spermatogenesis in the *Wnk1*$^{f/f}$; *Wnt7a-Cre* mice arrested primarily during the mid-pachynema stage in primary spermatocytes shortly after the onset of *Wnt7a-Cre*.

To focus on the populations with *Wnk1* ablation, we next re-clustered only the *Wnk1*-deficient germ cell populations (Figure 4H). Here, semi-supervised clustering and marker gene expression identified three main cell types in five clusters: spermatocytes (clusters SPCa and SPCb which were *Sycp1*/*Sycp2*/*Sycp3*-positive); round spermatids (clusters rSPTa and rSPTb which were *Ddx4*/*Catsper3*/*Catsper4*/*Acrv1*-positive); and elongating spermatids (cluster eSPT which was *Tnp1*/*Tnp2*/*Prm1*/*Prm3*/*Tssk6*/*Prm2*-positive and *Ddx4*-negative, Figures 4I and 4J).

Loss of *Wnk1* altered MTOR signaling during meiotic progression

Finally, we focused on the SPCa and SPCb clusters, in which *Wnt7a-Cre* expression was first detected. Differentially expressed genes (DEGs) in the SPCa and SPCb clusters between the *Wnk1*$^{f/f}$ and *Wnk1*$^{f/f}$; *Wnt7a-Cre* mice were identified based on adjusted p value < 0.05, base mean > 0.2, and Log (2) fold-change > 0.2 or < −0.2, which identified 2,323 DEGs (Table S1). Genes with the largest increase in mRNA abundance included the protamines (*Prm1* and *Prm2*), the transition nuclear proteins (*Tnp1* and *Tnp2*), the claudin protein *Cldn5*, zinc finger protein *Zfp637*, phospholipase protein *Pla2g12a*, CDC42 effector protein *Cdc42ep3*, acrosomal protein *Slxl1*, transcriptional regulator *Trim54*, calmodulin *Calm2*, kinase *Map4k1*, and translation initiation factor *Eif1b* (Table S2). Genes with the largest decrease in mRNA abundance were mitochondrial genes *mt-Nd1*, *mt-Nd2*, *mt-Nd3*, *mt-Nd4*, *mt-Cytb*, *mt-ATP6*, *mt-Co3*; RNA binding proteins *Cirbp*, *Hnrnpa2b1*, and *Rbm39*, the histone modifier *Ankrd12*, and endoplasmic reticulum related proteins *Erp29* and *Ssr2*. Many of these genes impacted by loss of WNK1 are either crucial for spermatogenesis or sperm function, including *Tnp1*, *Tnp2*, *Prm1*, *Prm2*, *Map4k1*, *Cldn5*, *Cirbp*, *Zfp637*, *Slxl1*, and *Ankrd12* (Table S2). Whereas some genes have been implicated in spermatogenesis, germ cell function or male fertility, their exact function remains to be determined (*mt-nd1*, *mt-cytb*, *Pla2g12a*, *Calm2*, *Erp29*, *Rbm39*, *mt-nd4*, *mt-nd3*, *mt-Atp6*, and *mt-nd2*), while others have not been reported in the male reproductive system (*Cdc43ep3*, *Trim54*, and *Eif1b*). In addition, several known meiotic regulators were also found to be impacted at the mRNA level in the *Wnk1*$^{f/f}$; *Wnt7a-Cre* spermatocytes (Table S3), including *Sycp1*, *Sycp2*, and *Sycp3* which form the axial and lateral elements of the synaptonemal complex during meiotic prophase I[35]; *Smc1b* which is critical for sister chromatid cohesion and DNA recombination,[36] *Atr* which mediates chromosome synapsis and DNA repair[37]; and *Aurkc* which is required for chromosome desynapsis and chromosome segregation.[38]

To obtain a global view of cellular functions impacted by WNK1 loss, the DEGs were systemically analyzed using bioinformatic tools including TopGO R Package (https://doi.org/10.18129/B9.bioc/topGO), ingenuity pathway analysis (IPA),[39] as well as gene set enrichments analysis (GSEA).[40,41] The gene ontology and pathway analyses unanimously ranked one of the top-most impacted events in the *Wnk1*$^{f/f}$; *Wnt7a-Cre* spermatocytes as "proteostasis maintaining function"—which included cytoplasmic translation, translation, peptide biosynthesis and metabolism, proteolysis, RNA binding and processing, and protein ubiquitination (Tables S4 and S5). Among those, translation initiation was one of the most positively enriched pathways as predicted by GSEA (Figure 5A), as well as EIF2 and EIF4 signaling, both of which are required for translation initiation (Table S5). Interestingly, our previous work indicated that WNK1 represses the major translation regulator MTOR in endometrial cells,[18] and upstream regulator analysis revealed several events correlating with upregulated MTOR signaling in the *Wnk1*$^{f/f}$; *Wnt7a-Cre* spermatocytes. These included significant positive *Z*-score for MTOR itself and its activator DDX5; as well as negative Z-scores for several MTOR repressors including sirolimus (rapamycin), torin1, UCHL1, and MAP4K4 (Figure 5B). The ribonucleoprotein LARP1, which is negatively regulated by MTOR and represses mRNA translation also exhibited a negative *Z*-score, supporting an elevation in MTOR signaling and translation.[42,43] In addition, several factors known to regulate translation also showed altered activity in the absence of WNK1, including KDM5A, DDX25, DDX3X, and the MYC proteins.

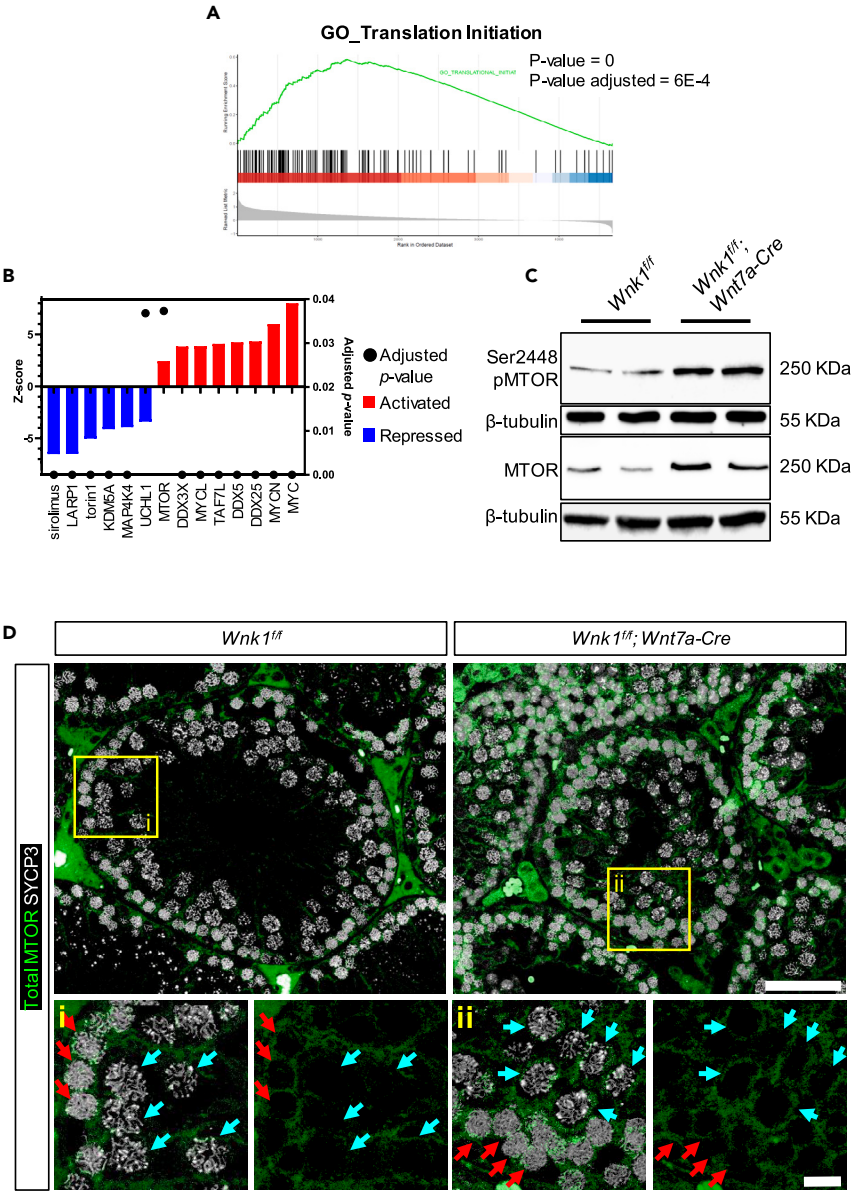

(figure continued on next page)

The predicted increase in MTOR and translation initiation represents a potential mechanism through which loss of WNK1 could impair spermatogenesis. To test this, we next examined MTOR levels in control and *Wnk1*$^{f/f}$*; Wnt7a-Cre* testes. Indeed, both phosphorylated and total MTOR protein levels were substantially elevated as shown by western blotting of whole-testis extracts (Figure 5C). This suggested that alterations to the MTOR pathway are primarily mediated at the expression level, and hence, we next focused on the total MTOR protein levels. To further examine the cell populations with increased MTOR expression, we dual-labeled the testicular cells with MTOR and SYCP3 to specifically examine MTOR levels in the spermatocytes using IF (Figure 5D). Owing to the high background signals observed, we included the secondary antibody only control in Figure S8 to confirm that intratubular signal were specific to the MTOR antibody (Figure S8). Since WNK1 is knocked-out during pachynema, we compared pre- and post-pachynema staged spermatocytes in stage XI tubules. In the control testis, MTOR is expressed in the zygotene spermatocytes while neighboring diplotene spermatocytes showed significantly reduced MTOR levels (Figure 5D i, red arrows and blue arrows indicate zygotene and diplotene spermatocytes, respectively). Similar MTOR expression is observed in the *Wnk1*$^{f/f}$*; Wnt7a-Cre* zygotene spermatocytes (Figure 5D ii, red arrows), however, the diplotene spermatocytes within the same tubule

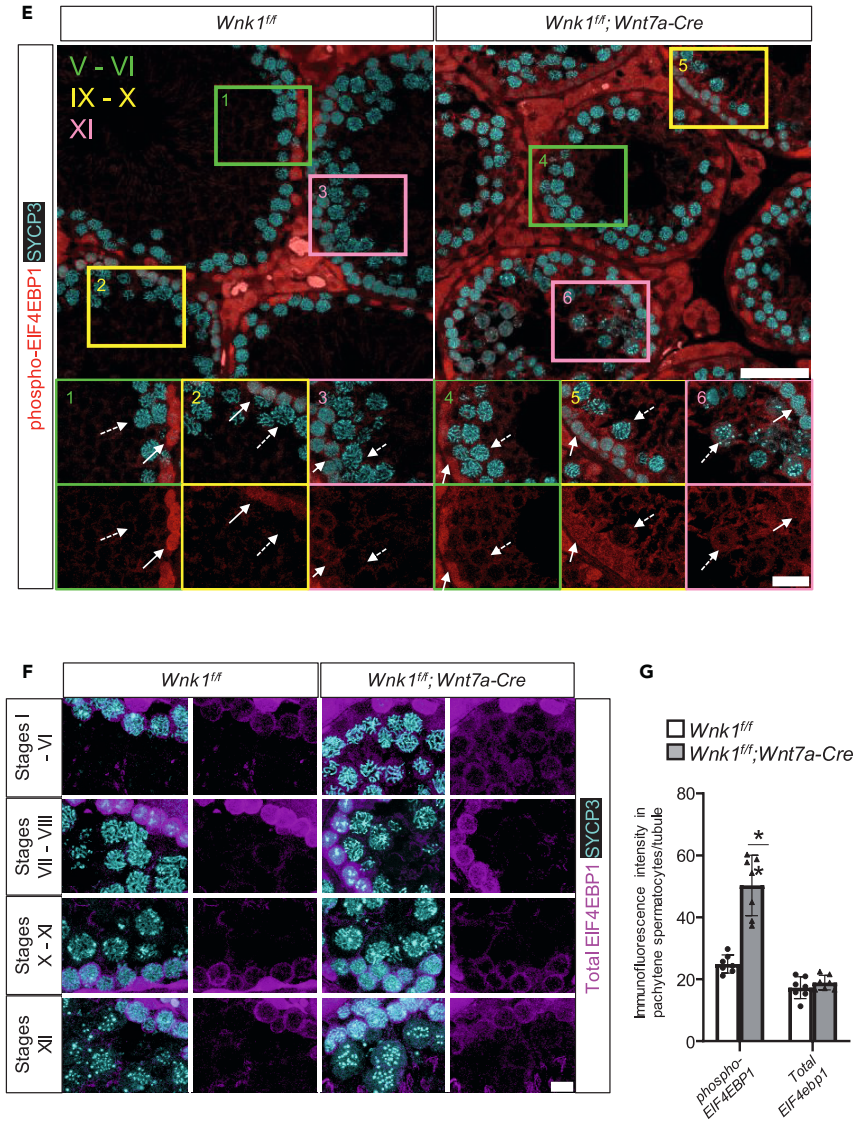

Figure 5. Loss of *Wnk1* altered MTOR signaling during meiotic progression

(A) Gene set enrichment analysis (GSEA) of the DEGs detected in cluster SPCa and SPCb from the scRNA-seq results, showing a positive enrichment of genes involved in translation initiation. All detected genes (Table S1) were ranked based on the fold changes (*Wnk1*$^{f/f}$; *Wnt7a-Cre* vs. *Wnk1*$^{f/f}$) from high (the left terminal of *X*-axis) to low (the right terminal of *X* axis).

(B) Activity of upstream regulators as predicted by IPA based on the SPCa and SPCb DEGs between the *Wnk1*$^{f/f}$ and *Wnk1*$^{f/f}$; *Wnt7a-Cre* mice. Blue = repressed, and red = activated (based on *Z*-score, left *Y* axis), and adjusted p values are shown on the right *Y* axis.

(C) Western blot showing MTOR and serine-2448 phosphorylated MTOR levels in the whole-testis lysate from the *Wnk1*$^{f/f}$ and *Wnk1*$^{f/f}$; *Wnt7a-Cre* mice. β-tubulin serves as loading control. (D) Total MTOR (green) immunostaining to show MTOR expression in stage XI tubule.

SYCP3 (white) was immunolabeled in parallel to identify zygotene (red arrows) and diplotene spermatocytes (blue arrows). Scale bar = 50 μm in the large image and 10 μm in insets.

(E) Phosphorylated EIF4EBP1 (red) was immunolabeled in parallel with SYCP3 (cyan) in the *Wnk1*$^{f/f}$ and *Wnk1*$^{f/f}$; *Wnt7a-Cre* testes. Insets 1 and 4 show B spermatogonia (solid arrows) and mid-stage pachytene spermatocytes (dashed arrows). Insets 2 and 5 show leptotene spermatocytes (solid arrow) and late-stage pachytene spermatocytes (dashed arrow); and insets 3 and 6 show zygotene spermatocytes (solid arrows) and diplotene spermatocytes (dashed arrow). Scale bars = 50 μm and 20 μm for the larger image and the insets, respectively.

(F) Total EIF4EBP1 (purple) was immunolabeled in parallel with SYCP3 (cyan) at different stages of the seminiferous cycle for the *Wnk1*$^{f/f}$ and *Wnk1*$^{f/f}$; *Wnt7a-Cre* testes. Scale bar = 10 μm.

(G) Quantification of IF signal intensity of phosphorylated and total EIF4EBP1 in SYCP3-positive cells from 7 tubules of 3 independent mice. Results shown are mean ± SD, **p < 0.001 based on two-tailed Student's *t* test.

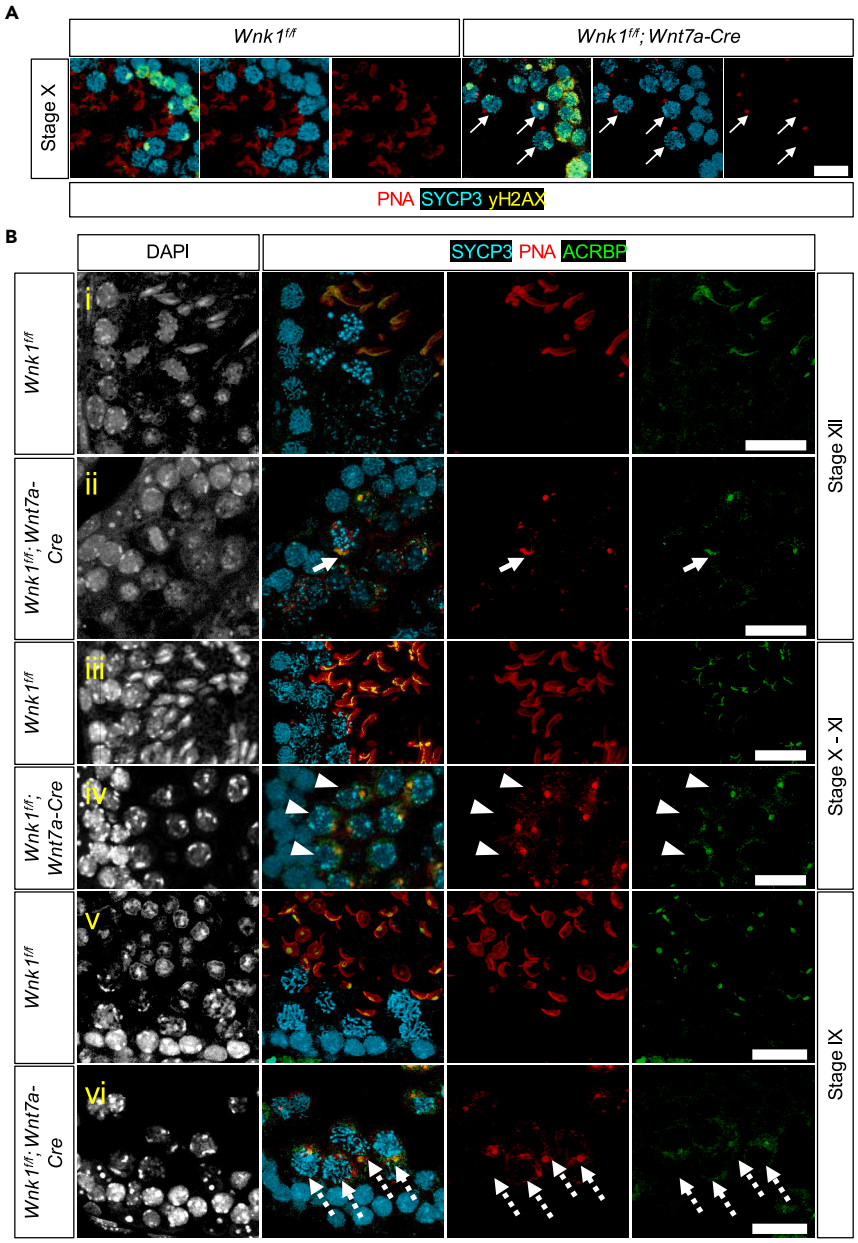

(figure continued on next page)

exhibited no reduction in MTOR level compared to their zygotene-staged predecessors (Figure 5D ii, blue arrows). These results confirmed that loss of WNK1 in mid-pachytene spermatocytes upregulated MTOR protein levels.

To examine whether elevated MTOR levels affected mTORC1 signaling, we next examined its phosphorylation target EIF4EBP1. In the EIF4-dependent translation initiation pathway, MTOR phosphorylates EIF4EBP1, and the phosphorylated EIF4EBP1 then releases EIF4E, which is freed to recruit 40S ribosomal subunit to the 5′ end of mRNAs, thereby initiating translation.[44] Hence, the degree of EIF4EBP1 phosphorylation is an indication of MTOR-mediated translational activity. We conducted IF to assess EIF4EBP1 phosphorylation level, and due to the high background signals observed, we included the secondary antibody only control in Figure S8 to confirm that intratubular signal were derived specifically from the phopho-EIF4EBP1 antibody (Figure S8). In the control testes, EIF4EBP1 is highly phosphorylated in SYCP3-negative spermatogonia (Figure 5E, inset 1, solid arrow). Phosphorylation decreased but was still detectable as spermatogonia progressed to leptonema and zygonema (Figure 5E, insets 2 and 3, solid arrows). By pachynema, EIF4EBP1 phosphorylation decreased to levels that were barely within detection range (Figure 5E, insets 1 and 2, dashed arrows). In the *Wnk1*$^{f/f}$*; Wnt7a-Cre* mice, spermatogonia, leptotene, and

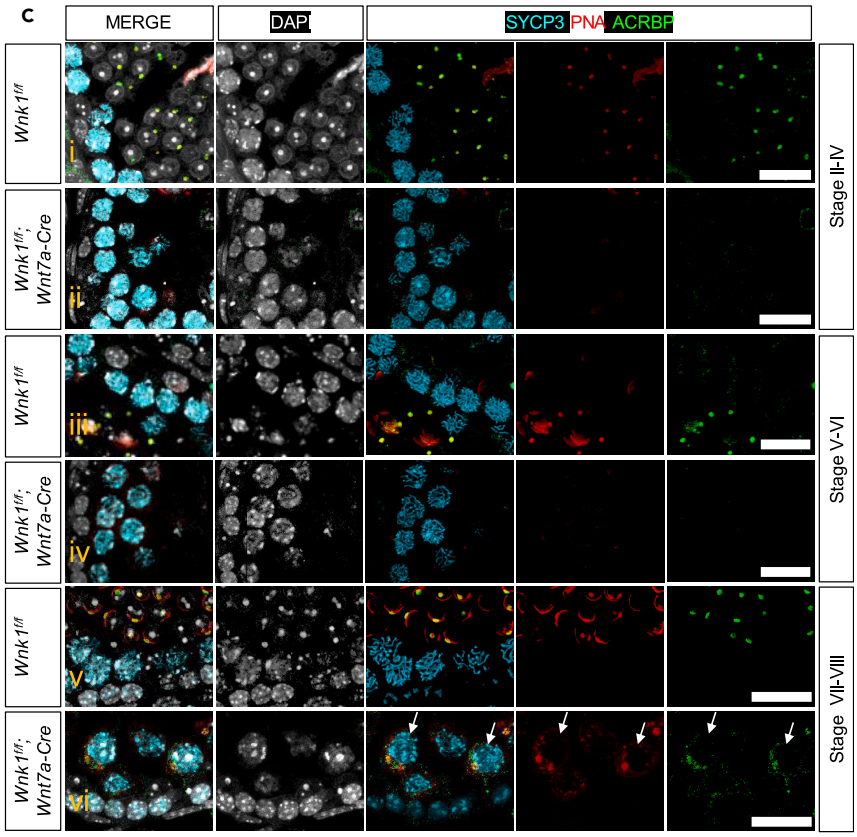

Figure 6. Premature expression of acrosomal protein ACRBP in the *Wnk1$^{f/f}$; Wnt7a-Cre* spermatocytes

(A) PNA binding (red) was examined in stage X tubules from the *Wnk1$^{f/f}$* and *Wnk1$^{f/f}$; Wnt7a-Cre* testes by IF in parallel with SYCP3 (cyan) and γH2AX (yellow). White arrows show pachytene spermatocytes with PNA staining in the *Wnk1$^{f/f}$; Wnt7a-Cre* mice. Scale bar = 20 μm.

(B) ACRBP (green), PNA (red) and SYCP3 (cyan) staining in *Wnk1$^{f/f}$* and *Wnk1$^{f/f}$; Wnt7a-Cre* testes at stages XII (subpanels i and ii), X–XI (subpanels iii and iv), and IX (subpanels v and vi). Arrow, arrowheads, and dashed arrows indicate ACRBP-positive meiotic cells at stages XII, XI, and IX, respectively. Scale bars = 20 μm.

(C) ACRBP (green), PNA (red) and SYCP3 (cyan) staining in *Wnk1$^{f/f}$* and *Wnk1$^{f/f}$; Wnt7a-Cre* testes at stages II–IV (subpanels i and ii), V–VI (subpanels iii and iv), and VII–VIII (subpanels v and vi). Arrows indicate the earliest detection of ACRBP expression in the *Wnk1$^{f/f}$; Wnt7a-Cre* testis. Scale bar = 20 μm.

zygotene spermatocytes showed similar levels of EIF4EBP1 phosphorylation as the control mice (Figure 5E, solid arrows in insets 4, 5, and 6). However, the high levels of EIF4EBP1 phosphorylation were maintained in *Wnk1$^{f/f}$; Wnt7a-Cre* pachytene spermatocytes (Figure 5E, insets 4 and 5, dashed arrows). This phosphorylation was maintained through pachynema, as diplotene spermatocytes still exhibited EIF4EBP1 phosphorylation (Figure 5E, inset 6, dashed arrow). In addition, when we examined total EIF4EBP1 levels in the spermatocytes at different stages of the seminiferous cycle, we found no obvious differences between the *Wnk1$^{f/f}$* and *Wnk1$^{f/f}$; Wnt7a-Cre* mice (Figure 5F). These visual observations were confirmed by IF signal intensity quantification using the FIJI software (Figure 5G). Hence, the increase in EIF4EBP1 phosphorylation was likely due to elevated mTORC1 signaling and not increase in total EIF4EBP1 level. In addition, the elevated level of EIF4EBP1 phosphorylation supported the idea that loss of *Wnk1* from the spermatocytes could impact translation.

Premature expression of acrosomal protein ACRBP in the *Wnk1$^{f/f}$; Wnt7a-Cre* spermatocytes

Translation control is an important gene expression regulatory mechanism in spermatogenic cells due to the transcriptional "shut-down", which occurs during the homologous chromosome recombination in prophase of meiosis I, as well as the chromatin condensation phase during spermiogenesis.[45,46] As such, germ cells transcribe genes that are required for these transcriptionally inert stages and store them as translationally repressed until needed. Based on our findings that loss of WNK1 increased mTORC1 signaling, we postulated that this might cause increase in protein synthesis, leading to premature mRNA translation. To test this possibility, we examined the post-meiotically synthesized acrosome to see if premature expression is detected in the *Wnk1$^{f/f}$; Wnt7a-Cre* spermatocytes. First, we used PNA which binds to the acrosome membrane to assess the acrosomal status.[26] We found that in the *Wnk1$^{f/f}$; Wnt7a-Cre* testis, PNA staining was already observed in late-stage pachytene spermatocytes (Figure 6A, white arrows), suggesting that the acrosomal components were possibly expressed prior to meiotic completion. Although this was an exciting observation, we could not rule out the possibility that premature PNA binding was associated with defects in carbohydrate biosynthesis or secretion as PNA can also bind carbohydrates. To determine whether the PNA staining

detected in the *Wnk1*$^{f/f}$*; Wnt7a-Cre* spermatocytes were acrosome-like structures, we next immunolabeled actual acrosomal components—the acrosin binding protein (ACRBP), the sperm equatorial segment protein 1 (SPESP1), and the acrosomal vesicle protein 1 (ACRV1) and detected their expression via IF in the *Wnk1*$^{f/f}$ and the *Wnk1*$^{f/f}$*; Wnt7a-Cre* testes. While we could not detect premature SPESP1 and ACRV1 expression in *Wnk1*$^{f/f}$*; Wnt7a-Cre* testes (Figure S9), ACRBP was indeed, prematurely expressed in the spermatocytes (Figures 6B and 6C). In the *Wnk1*$^{f/f}$*; Wnt7a-Cre* testes, both PNA and ACRBP were detected in metaphase I spermatocytes (Figure 6B, panel ii, white arrow), whereas none were present in the metaphase I spermatocytes from the control testes (Figure 6B, panel i). We further examined diplotene and late-pachytene spermatocytes in stage IX–XI tubules and found that ACRBP was also present at this stage in the *Wnk1*$^{f/f}$*; Wnt7a-Cre* testes (Figure 6B, panels iii–vi, ACRBP-positive spermatocytes are indicated by arrows). Additionally, colocalization of ACRBP and PNA signal indicated that the PNA signal likely corresponded to the acrosome-like structure. Last, we examined early and mid-pachytene spermatocytes to determine when ACRBP was first expressed. No ACRBP was detected in spermatocytes between stages II and VI (Figure 6C, panels i–iv), and the first sign of ACRBP expression was in stage VII–VIII spermatocytes shortly after *Wnt7a-Cre* onset (Figure 6C, panel vi, arrows). Taken together, these results demonstrate that loss of *Wnk1* in the spermatocytes elevated MTOR expression and mTORC1 signaling. This was associated with increased EIF4EBP1 phosphorylation, and the premature expression of the acrosomal component ACRBP.

DISCUSSION

In this study, we report our fortuitous discovery that WNK1 is required for spermatogenesis and male fertility through a combination of two unexpected events. First, we demonstrate that *Wnt7a*, a *Cre* driver that was previously established for gene recombination in the uterine epithelium,[21] is also expressed in the male germline, causing gene recombination in the male gametes. Combining a series of studies using reporter mice, we pinpoint the onset of *Wnt7a-Cre* to mid-stage pachytene spermatocytes. This unreported male germline *Cre* demonstrates consistency and efficiency, which will be a valuable tool for studying spermatogenesis as current germline *Cre* models are often compromised by leakiness. Furthermore, the precise onset in mid-pachytene spermatocytes provides a useful tool to study spermatogenic meiosis during the lengthy pachynema stage with a higher temporal resolution.

Our second finding is that WNK1 is indispensable for spermatogenesis. Interestingly, multiple studies have demonstrated that testes exhibit the highest WNK1 expression when compared to other organs in humans, mice, and rats.[22,23,47] Further, it was shown that the WNK1 isoform expressed in the testis contains the kinase domain, indicating that it likely drives spermatogenic functions via its kinase activity.[23] Indeed, a more recent study showed that WNK1 is one of the kinases exhibiting the highest phosphorylation level based on human testis phosphoproteome profiling.[48] In the current study, we show that WNK1 depletion in mid-pachytene spermatocytes resulted in male infertility. This was due to failure to complete spermatogenesis, and we further determined that the primary arrest occurred during mid-pachynema in the primary spermatocytes. It is worth noting that some cells do escape this primary arrest, as we did observe round spermatids in the *Wnk1*$^{f/f}$*; Wnt7a-Cre* testes, albeit at low quantities. Despite this, the epididymides were completely devoid of sperm, which suggested that WNK1 likely have additional post-meiotic functions which impeded further development of the "escaped" round spermatids. Indeed, although not discussed herein, WNK1 protein was also observed in the elongated spermatids based on IHC staining (Figures 1D, S1, and S2). The potential pleiotropic function of WNK1 in regulating multiple stages of spermatogenesis is exciting and worth further exploring in the future.

Single-cell transcriptomic profiling supported our histological evaluations that firstly, the onset of *Wnt7a-Cre* was in the meiotic spermatocyte population, and secondly, *Wnt7a-Cre* onset rapidly caused spermatogenic arrest, as both events were observed in the SPC3/SPCa cluster. Interestingly, single-cell profiling also detected a small population of elongated spermatids in the *Wnk1*$^{f/f}$*; Wnt7a-Cre* mice despite a complete absence in our histological examinations (Figures 4F and 4G–4J). We speculate that this may be due to the round spermatids progressing transcriptionally but failing to undergo the morphogenetic program to form elongated spermatids, thereby forming cells with transcriptomic profiles resembling that of elongated spermatids but still exhibiting round-spermatid morphology. Comparison of the mid-pachytene spermatocytes (where the primary arrest occurred) between the *Wnk1*$^{f/f}$ and *Wnk1*$^{f/f}$*; Wnt7a-Cre* mice revealed that loss of *Wnk1* increased MTOR signaling. This was observed with a concomitant increase in EIF4EBP1 phosphorylation, a direct target of MTOR in the mTORC1 translation pathway. Hence, we further hypothesized that translation may be accelerated in the *Wnk1*-depleted spermatocytes.[49] This was supported by our finding that premature expression of the acrosomal protein ACRBP was observed in the *Wnk1*-depleted spermatocytes. Translation is a critically controlled process in maturing male germ cells to prevent premature expression of stored mRNAs,[45,46,50] and this is carefully orchestrated at multiple levels (including post-transcriptional and translational) to ensure temporally appropriate protein expression.[51–55] The identification of WNK1's regulatory impact on MTOR and EIF4EBP1 suggested that WNK1 may mediate translation in spermatocytes via the MTOR pathway. As MTOR is a major regulator of translation, we also speculate that loss of *Wnk1*-induced MTOR upregulation likely impacts translation for multiple mRNAs. However, there appeared to be some selectivity, as we did not observe premature translation for *Acrv1* and *Spesp1*. To further understand the potential role of WNK1 in translation, an obvious future direction is to identify the subset of mRNAs whose translation is impacted by the loss of *Wnk1* via polysome profiling and ribosome sequencing. Comparison of the structures of these transcripts, for instance, the 5′ and 3′ UTRs, as well as the poly(A) tail length and modifications may provide insights into how translation of these mRNAs are regulated. While disrupted translation in the male germline is detrimental to spermatogenesis, and premature expression of several proteins has been shown to compromise spermatogenesis and fertility,[56–58] whether premature expression of ACRBP was actually the causing factor for spermatogenic failure in the *Wnk1*$^{f/f}$*; Wnt7a-Cre* mice, and whether this was associated with increased MTOR signaling remain to be validated.

The mechanism underlying WNK1's regulation of MTOR is another interesting avenue to explore. In our previous study, we found that MTOR was also repressed by WNK1 in the female reproductive tract.[18] This indicated that the regulatory function of WNK1 on the MTOR

pathway may exist in other tissues. Although the exact molecular mechanisms underlying how WNK1 regulates MTOR signaling remains to be elucidated, our data suggest that in the male germline, the primary modulatory node is at the MTOR protein expression level. Further, we speculate that the increased MTOR protein level with loss of *Wnk1* is likely (or at least partially) mediated at the mRNA level. This is based on the scRNA-seq data which indicated a significant upregulation of *Mtor* in *Wnk1*$^{f/f}$*; Wnt7a-Cre* spermatocytes compared to control spermatocytes (Table S1). This means that under normal conditions, WNK1 may repress *Mtor* transcription or accelerate *Mtor* mRNA decay, and hence, loss of WNK1 resulted in increased *Mtor* transcripts. Another interesting aspect of our study is that most studies aimed at understanding the function of MTOR in spermatogenesis examines how loss of MTOR impacts germline development and function using genetic or pharmacological methods, and little is known about how overexpression of MTOR or how elevated mTORC1 signaling impact germline development and function *in vivo*.

While MTOR signaling (and possibly translation) appeared to be one of the impacted biological processes in the absence of WNK1, other yet-unexplored possibilities should also be considered. Based on DEGs in the mid-pachytene spermatocytes, another obvious candidate is the mitochondria—as expression of many mitochondrial genes were severely impacted in the *Wnk1*$^{f/f}$*; Wnt7a-Cre* spermatocytes (Table S2), and "oxidative phosphorylation" and "mitochondrial dysfunction" were also among the topmost significantly impacted pathways (Table S5). Mitochondrial functionality is a critical factor in male fertility in multiple aspects, including energy metabolism and DNA condensation.[59] It would be interesting to assess mitochondrial biology in the *Wnk1*$^{f/f}$*; Wnt7a-Cre* mice to understand whether WNK1 is associated with mitochondrial function in the male germline. Another feasibility is that loss of WNK1 led to infertility via dysregulated PP2A phosphatase activity in the spermatocytes. This is a signaling axis we previously elucidated in uterine cells, where *Wnk1* deletion led to decreased expression of multiple PP2A subunits, which in turn impacted AKT and FOXO1 phosphorylation.[18] Intriguingly, others have found that germline knockout of PP2A components similarly led to meiotic impairment and male infertility in mouse models.[60,61] Hence, it's possible that in the *Wnk1*$^{f/f}$*; Wnt7a-Cre* mice, the infertility is associated with PP2A dysfunction, however, this possibility must also be validated. Lastly, DEG analysis between the *Wnk1*$^{f/f}$ and *Wnk1*$^{f/f}$*; Wnt7a-Cre* spermatocytes revealed a multitude of dysregulated genes with reported roles in male germ cell development and function. For example, *Tekt4*, *Ropn1*, *Ropn1l*, *Akap3*, *Iqub*, *Sord*, *Tssk1*, *Odf2*, and *Catsperg2* are required for normal sperm morphology and motility[62–66]; *Odf1* is crucial for sperm head-tail coupling[67]; *Adam3* and *Spa17* are required for sperm migration and sperm binding to zona pellucida[65,68]; and *Cadm1* which is required for germ cell adhesion to Sertoli cells.[69] The altered expression of these genes suggests WNK1 could regulate other aspects of male fertility. Although these observations provide novel directions for future exploration, these speculations require further verification at the protein level.

With everything considered, it is also possible that ablation of WNK1 in the spermatocytes impacted multiple signaling pathways and functions, which cumulatively resulted in male infertility. Nonetheless, WNK1's criticality in spermatogenesis is solidly established in this study. Further, identification of WNK1 as a regulator of MTOR is pertinent as both WNK1 and MTOR are ubiquitously expressed. Understanding WNK1's molecular mechanisms and subcellular functions in the germ cells could be extrapolated to other systems where WNK1 is also expressed and functional to provide potential insights into WNK1's function and WNK1-dysregulation induced disease states. Future studies will combine WNK1 phosphoproteome profiling and immunoprecipitation coupled to mass spectrometry to identify WNK1's direct targets in the male germline, and expand the network from there.

In conclusion, impaired fertility and reproductive diseases affect a significant portion of our population. Understanding how the germline functions by identifying and defining critical regulators will aid in the future treatment of fertility issues and germline-related diseases. Furthermore, the identification of WNK1, as well as mediators in the WNK1 signaling network will increase the repertoire of diagnostic and therapeutic tools or targets for the clinical management of male fertility and contraception.

LIMITATIONS OF THE STUDY

In this study, we showed that the kinase protein WNK1 is indispensable for spermatogenesis and male fertility. The deletion of *Wnk1* during mid-pachynema rapidly led to spermatogenic arrest prior to meiotic completion. We found that in the *Wnk1*-depleted spermatocytes, there was increased MTOR protein expression and increased mTORC1 signaling (as indicated by increased phosphorylation of EIF4EBP1, a direct MTOR target). Concomitantly, we found premature expression of the acrosomal protein ACRBP, which supported our hypothesis that WNK1 elevated mTORC1 signaling, ultimately resulting in increased translation. The major scientific limitation of the current study is that we do not understand the mechanism underlying how WNK1 modulate MTOR expression. In addition, the association between increased mTORC1 signaling and premature expression of ACRBP must be examined in more depth to establish the causal relationship for these two events. One technical limitation of the study is that we used a non-standard approach of combining tubule staging and γH2AX/SYCP3 expression to determine cell identity.

STAR★METHODS

Detailed methods are provided in the online version of this paper and include the following:

- KEY RESOURCES TABLE
- RESOURCE AVAILABILITY
  - Lead contact
  - Materials availability
  - Data and code availability

SUPPLEMENTAL INFORMATION

Supplemental information can be found online at https://doi.org/10.1016/j.isci.2023.107616.

ACKNOWLEDGMENTS

The authors thank Zhao Fei for initial guidance and Marine Baptissart for assisting with the gene ontology analysis and sharing the ribosome illustration for the graphical abstract. We thank Sylvia Hewitt, Humphrey Yao, and Manas Ray for reviewing the manuscript. We appreciate support from the NIEHS animal facility, the Knockout Mouse Core, the Digital Imaging Core, the Bioinformatics Support Group, the Epigenomics and DNA Sequencing Core and the Fluorescent Microscopy and Imaging Core of NIEHS for their support and guidance with specialized techniques. Finally, we used illustrations ("Intracellular components") from Servier Medical Art by Servier, licensed under a Creative Commons Attribution 3.0 Unported License (https://creativecommons.org/licenses/by/3.0/) for the graphical abstract. This study was supported by the NIH grant ZIAES103311 to FJD, ZIAES103339 to MM, and R01 DK111542 to CLH.

AUTHOR CONTRIBUTIONS

Conceptualization: R.A.C., F.D.
Methodology: R.A.C., X.X., Xin.Xu., G.H., P.B., O.K., C.G.,
Investigation: R.A.C., X.X., C.W.
Visualization: R.A.C., J.L., G.H., C.G., M.M.
Supervision: R.A.C., J.L., M.M., F.D.
Writing—original draft: R.A.C.
Writing—review & editing: R.A.C., C.G., M.M., F.D.

DECLARATION OF INTERESTS

The authors declare no competing interests.

Received: December 19, 2022
Revised: June 4, 2023
Accepted: August 9, 2023
Published: August 12, 2023

REFERENCES

1. Kumar, N., and Singh, A.K. (2015). Trends of male factor infertility, an important cause of infertility: A review of literature. J. Hum. Reprod. Sci. *8*, 191–196. https://doi.org/10.4103/0974-1208.170370.
2. Levine, H., Jørgensen, N., Martino-Andrade, A., Mendiola, J., Weksler-Derri, D., Jolles, M., Pinotti, R., and Swan, S.H. (2022). Temporal trends in sperm count: a systematic review and meta-regression analysis of samples collected globally in the 20th and 21st centuries. Hum. Reprod. Update *29*, 157–176. https://doi.org/10.1093/humupd/dmac035.
3. Boivin, J., Bunting, L., Collins, J.A., and Nygren, K.G. (2007). International estimates of infertility prevalence and treatment-seeking: potential need and demand for infertility medical care. Hum. Reprod. *22*, 1506–1512. https://doi.org/10.1093/humrep/dem046.
4. Fainberg, J., and Kashanian, J.A. (2019). Recent advances in understanding and managing male infertility. F1000Res. *8*. https://doi.org/10.12688/f1000research.17076.1.
5. Nagase, T., Ishikawa, K., Nakajima, D., Ohira, M., Seki, N., Miyajima, N., Tanaka, A., Kotani, H., Nomura, N., and Ohara, O. (1997). Prediction of the coding sequences of unidentified human genes. VII. The complete sequences of 100 new cDNA clones from brain which can code for large proteins in vitro. DNA Res. *4*, 141–150. https://doi.org/10.1093/dnares/4.2.141.
6. Disse-Nicodème, S., Achard, J.M., Desitter, I., Houot, A.M., Fournier, A., Corvol, P., and Jeunemaitre, X. (2000). A new locus on chromosome 12p13.3 for pseudohypoaldosteronism type II, an autosomal dominant form of hypertension. Am. J. Hum. Genet. *67*, 302–310. https://doi.org/10.1086/303020.
7. Lafreniere, R.G., MacDonald, M.L.E., Dube, M.P., MacFarlane, J., O'Driscoll, M., Brais, B., Meilleur, S., Brinkman, R.R., Dadivas, O., Pape, T., et al. (2004). Identification of a novel gene (HSN2) causing hereditary sensory and autonomic neuropathy type II through the Study of Canadian Genetic Isolates. Am. J. Hum. Genet. *74*, 1064–1073. https://doi.org/10.1086/420795.
8. Xie, J., Wu, T., Xu, K., Huang, I.K., Cleaver, O., and Huang, C.L. (2009). Endothelial-specific expression of WNK1 kinase is essential for angiogenesis and heart development in mice. Am. J. Pathol. *175*, 1315–1327. https://doi.org/10.2353/ajpath.2009.090094.
9. Xie, J., Yoon, J., Yang, S.S., Lin, S.H., and Huang, C.L. (2013). WNK1 protein kinase regulates embryonic cardiovascular development through the OSR1 signaling cascade. J. Biol. Chem. *288*, 8566–8574. https://doi.org/10.1074/jbc.M113.451575.
10. Adams, N.R., Vasquez, Y.M., Mo, Q., Gibbons, W., Kovanci, E., and DeMayo, F.J. (2017). WNK lysine deficient protein kinase 1 regulates human endometrial stromal cell decidualization, proliferation, and migration in part through mitogen-activated protein kinase 7. Biol. Reprod. *97*, 400–412. https://doi.org/10.1093/biolre/iox108.
11. Gallolu Kankanamalage, S., Lee, A.Y., Wichaidit, C., Lorente-Rodriguez, A., Shah, A.M., Stippec, S., Whitehurst, A.W., and Cobb, M.H. (2016). Multistep regulation of autophagy by WNK1. Proc. Natl. Acad. Sci. USA *113*, 14342–14347. https://doi.org/10.1073/pnas.1617649113.
12. Oh, E., Heise, C.J., English, J.M., Cobb, M.H., and Thurmond, D.C. (2007). WNK1 is a novel regulator of Munc18c-syntaxin 4 complex formation in soluble NSF attachment protein receptor (SNARE)-mediated vesicle exocytosis. J. Biol. Chem. *282*, 32613–32622. https://doi.org/10.1074/jbc.M706591200.
13. Volanakis, A., Kamieniarz-Gdula, K., Schlackow, M., and Proudfoot, N.J. (2017). WNK1 kinase and the termination factor PCF11 connect nuclear mRNA export with transcription. Genes Dev. *31*, 2175–2185. https://doi.org/10.1101/gad.303677.117.
14. Mitsopoulos, C., Zihni, C., Garg, R., Ridley, A.J., and Morris, J.D.H. (2003). The prostate-derived sterile 20-like kinase (PSK) regulates microtubule organization and stability. J. Biol. Chem. *278*, 18085–18091. https://doi.org/10.1074/jbc.M213064200.
15. Tu, S.W., Bugde, A., Luby-Phelps, K., and Cobb, M.H. (2011). WNK1 is required for mitosis and abscission. Proc. Natl. Acad. Sci. USA *108*, 1385–1390. https://doi.org/10.1073/pnas.1018567108.
16. Pleiner, T., Hazu, M., Tomaleri, G.P., Januszyk, K., Oania, R.S., Sweredoski, M.J., Moradian, A., Guna, A., and Voorhees, R.M. (2021). WNK1 is an assembly factor for the human ER membrane protein complex. Mol. Cell *81*, 2693–2704.e12. https://doi.org/10.1016/j.molcel.2021.04.013.
17. Large, M.J., Wetendorf, M., Lanz, R.B., Hartig, S.M., Creighton, C.J., Mancini, M.A., Kovanci, E., Lee, K.F., Threadgill, D.W., Lydon, J.P., et al. (2014). The epidermal growth factor receptor critically regulates endometrial function during early pregnancy. PLoS Genet. *10*, e1004451. https://doi.org/10.1371/journal.pgen.1004451.
18. Chi, R.P.A., Wang, T., Huang, C.L., Wu, S.P., Young, S.L., Lydon, J.P., and DeMayo, F.J. (2020). WNK1 regulates uterine homeostasis and its ability to support pregnancy. JCI Insight *5*, e141832. https://doi.org/10.1172/jci.insight.141832.
19. Morgan, M., Kumar, L., Li, Y., and Baptissart, M. (2021). Post-transcriptional regulation in spermatogenesis: all RNA pathways lead to healthy sperm. Cell. Mol. Life Sci. *78*, 8049–8071. https://doi.org/10.1007/s00018-021-04012-4.
20. Bettegowda, A., and Wilkinson, M.F. (2010). Transcription and post-transcriptional regulation of spermatogenesis. Philos. Trans. R. Soc. Lond. B Biol. Sci. *365*, 1637–1651. https://doi.org/10.1098/rstb.2009.0196.
21. Winuthayanon, W., Hewitt, S.C., Orvis, G.D., Behringer, R.R., and Korach, K.S. (2010). Uterine epithelial estrogen receptor alpha is dispensable for proliferation but essential for complete biological and biochemical responses. Proc. Natl. Acad. Sci. USA *107*, 19272–19277. https://doi.org/10.1073/pnas.1013226107.
22. Moore, T.M., Garg, R., Johnson, C., Coptcoat, M.J., Ridley, A.J., and Morris, J.D. (2000). PSK, a novel STE20-like kinase derived from prostatic carcinoma that activates the c-Jun N-terminal kinase mitogen-activated protein kinase pathway and regulates actin cytoskeletal organization. J. Biol. Chem. *275*, 4311–4322. https://doi.org/10.1074/jbc.275.6.4311.
23. O'Reilly, M., Marshall, E., Speirs, H.J.L., and Brown, R.W. (2003). WNK1, a gene within a novel blood pressure control pathway, tissue-specifically generates radically different isoforms with and without a kinase domain. J. Am. Soc. Nephrol. *14*, 2447–2456. https://doi.org/10.1097/01.asn.0000089830.97681.3b.
24. Hogarth, C.A., Evanoff, R., Mitchell, D., Kent, T., Small, C., Amory, J.K., and Griswold, M.D. (2013). Turning a spermatogenic wave into a tsunami: synchronizing murine spermatogenesis using WIN 18,446. Biol. Reprod. *88*, 40. https://doi.org/10.1095/biolreprod.112.105346.
25. Romer, K.A., de Rooij, D.G., Kojima, M.L., and Page, D.C. (2018). Isolating mitotic and meiotic germ cells from male mice by developmental synchronization, staging, and sorting. Dev. Biol. *443*, 19–34. https://doi.org/10.1016/j.ydbio.2018.08.009.
26. Mortimer, D., Curtis, E.F., and Miller, R.G. (1987). Specific labelling by peanut agglutinin of the outer acrosomal membrane of the human spermatozoon. J. Reprod. Fertil. *81*, 127–135. https://doi.org/10.1530/jrf.0.0810127.
27. Muzumdar, M.D., Tasic, B., Miyamichi, K., Li, L., and Luo, L. (2007). A global double-fluorescent Cre reporter mouse. Genesis *45*, 593–605. https://doi.org/10.1002/dvg.20335.
28. Mo, A., Mukamel, E.A., Davis, F.P., Luo, C., Henry, G.L., Picard, S., Urich, M.A., Nery, J.R., Sejnowski, T.J., Lister, R., et al. (2015). Epigenomic Signatures of Neuronal Diversity in the Mammalian Brain. Neuron *86*, 1369–1384. https://doi.org/10.1016/j.neuron.2015.05.018.
29. Blanco-Rodríguez, J. (2009). gammaH2AX marks the main events of the spermatogenic process. Microsc. Res. Tech. *72*, 823–832. https://doi.org/10.1002/jemt.20730.
30. Inselman, A.L., Nakamura, N., Brown, P.R., Willis, W.D., Goulding, E.H., and Eddy, E.M. (2010). Heat shock protein 2 promoter drives Cre expression in spermatocytes of transgenic mice. Genesis *48*, 114–120. https://doi.org/10.1002/dvg.20588.
31. John, G.B., Gallardo, T.D., Shirley, L.J., and Castrillon, D.H. (2008). Foxo3 is a PI3K-dependent molecular switch controlling the initiation of oocyte growth. Dev. Biol. *321*, 197–204. https://doi.org/10.1016/j.ydbio.2008.06.017.
32. Shaha, C., Tripathi, R., and Mishra, D.P. (2010). Male germ cell apoptosis: regulation and biology. Philos. Trans. R. Soc. Lond. B Biol. Sci. *365*, 1501–1515. https://doi.org/10.1098/rstb.2009.0124.
33. Hermann, B.P., Cheng, K., Singh, A., Roa-De La Cruz, L., Mutoji, K.N., Chen, I.C., Gildersleeve, H., Lehle, J.D., Mayo, M., Westernströer, B., et al. (2018). The Mammalian Spermatogenesis Single-Cell Transcriptome, from Spermatogonial Stem Cells to Spermatids. Cell Rep. *25*, 1650–1667.e8. https://doi.org/10.1016/j.celrep.2018.10.026.
34. Qiu, X., Mao, Q., Tang, Y., Wang, L., Chawla, R., Pliner, H.A., and Trapnell, C. (2017). Reversed graph embedding resolves complex single-cell trajectories. Nat. Methods *14*, 979–982. https://doi.org/10.1038/nmeth.4402.
35. Schramm, S., Fraune, J., Naumann, R., Hernandez-Hernandez, A., Höög, C., Cooke, H.J., Alsheimer, M., and Benavente, R. (2011). A novel mouse synaptonemal complex protein is essential for loading of central element proteins, recombination, and fertility. PLoS Genet. *7*, e1002088. https://doi.org/10.1371/journal.pgen.1002088.
36. Revenkova, E., Eijpe, M., Heyting, C., Hodges, C.A., Hunt, P.A., Liebe, B., Scherthan, H., and Jessberger, R. (2004). Cohesin SMC1β is

required for meiotic chromosome dynamics, sister chromatid cohesion and DNA recombination. Nat. Cell Biol. *6*, 555–562. https://doi.org/10.1038/ncb1135.

37. Widger, A., Mahadevaiah, S.K., Lange, J., Ellnati, E., Zohren, J., Hirota, T., Pacheco, S., Maldonado-Linares, A., Stanzione, M., Ojarikre, O., et al. (2018). ATR is a multifunctional regulator of male mouse meiosis. Nat. Commun. *9*, 2621. https://doi.org/10.1038/s41467-018-04850-0.
38. Wellard, S.R., Schindler, K., and Jordan, P.W. (2020). Aurora B and C kinases regulate chromosome desynapsis and segregation during mouse and human spermatogenesis. J. Cell Sci. *133*, jcs248831. https://doi.org/10.1242/jcs.248831.
39. Krämer, A., Green, J., Pollard, J., Jr., and Tugendreich, S. (2013). Causal analysis approaches in Ingenuity Pathway Analysis. Bioinformatics *30*, 523–530. https://doi.org/10.1093/bioinformatics/btt703.
40. Mootha, V.K., Lindgren, C.M., Eriksson, K.F., Subramanian, A., Sihag, S., Lehar, J., Puigserver, P., Carlsson, E., Ridderstråle, M., Laurila, E., et al. (2003). PGC-1alpha-responsive genes involved in oxidative phosphorylation are coordinately downregulated in human diabetes. Nat. Genet. *34*, 267–273. https://doi.org/10.1038/ng1180.
41. Subramanian, A., Tamayo, P., Mootha, V.K., Mukherjee, S., Ebert, B.L., Gillette, M.A., Paulovich, A., Pomeroy, S.L., Golub, T.R., Lander, E.S., and Mesirov, J.P. (2005). Gene set enrichment analysis: a knowledge-based approach for interpreting genome-wide expression profiles. Proc. Natl. Acad. Sci. USA *102*, 15545–15550. https://doi.org/10.1073/pnas.0506580102.
42. Philippe, L., Vasseur, J.-J., Debart, F., and Thoreen, C.C. (2018). La-related protein 1 (LARP1) repression of TOP mRNA translation is mediated through its cap-binding domain and controlled by an adjacent regulatory region. Nucleic Acids Res. *46*, 1457–1469. https://doi.org/10.1093/nar/gkx1237.
43. Hong, S., Freeberg, M.A., Han, T., Kamath, A., Yao, Y., Fukuda, T., Suzuki, T., Kim, J.K., and Inoki, K. (2017). LARP1 functions as a molecular switch for mTORC1-mediated translation of an essential class of mRNAs. Elife *6*, e25237. https://doi.org/10.7554/eLife.25237.
44. Karim, M.M., Hughes, J.M., Warwicker, J., Scheper, G.C., Proud, C.G., and McCarthy, J.E. (2001). A quantitative molecular model for modulation of mammalian translation by the eIF4E-binding protein 1. J. Biol. Chem. *276*, 20750–20757. https://doi.org/10.1074/jbc.M011068200.
45. Monesi, V. (1964). Ribonucleic acid synthesis during mitosis and meiosis in the mouse testis. J. Cell Biol. *22*, 521–532. https://doi.org/10.1083/jcb.22.3.521.
46. Turner, J.M.A., Mahadevaiah, S.K., Fernandez-Capetillo, O., Nussenzweig, A., Xu, X., Deng, C.X., and Burgoyne, P.S. (2005). Silencing of unsynapsed meiotic chromosomes in the mouse. Nat. Genet. *37*, 41–47. https://doi.org/10.1038/ng1484.
47. Vitari, A.C., Deak, M., Morrice, N.A., and Alessi, D.R. (2005). The WNK1 and WNK4 protein kinases that are mutated in Gordon's hypertension syndrome phosphorylate and activate SPAK and OSR1 protein kinases. Biochem. J. *391*, 17–24. https://doi.org/10.1042/bj20051180.
48. Castillo, J., Knol, J.C., Korver, C.M., Piersma, S.R., Pham, T.V., de Goeij-de Haas, R.R., van Pelt, A.M.M., Jimenez, C.R., and Jansen, B.J.H. (2019). Human Testis Phosphoproteome Reveals Kinases as Potential Targets in Spermatogenesis and Testicular Cancer. Mol. Cell. Proteomics *18*. S132–s144. https://doi.org/10.1074/mcp.RA118.001278.
49. Gingras, A.C., Kennedy, S.G., O'Leary, M.A., Sonenberg, N., and Hay, N. (1998). 4E-BP1, a repressor of mRNA translation, is phosphorylated and inactivated by the Akt(PKB) signaling pathway. Genes Dev. *12*, 502–513. https://doi.org/10.1101/gad.12.4.502.
50. Hecht, N.B. (1998). Molecular mechanisms of male germ cell differentiation. Bioessays *20*, 555–561. https://doi.org/10.1002/(sici)1521-1878(199807)20:7<555::Aid-bies6>3.0.Co;2-j.
51. Jamsai, D., O'Connor, A.E., O'Donnell, L., Lo, J.C.Y., and O'Bryan, M.K. (2015). Uncoupling of transcription and translation of Fanconi anemia (FANC) complex proteins during spermatogenesis. Spermatogenesis *5*, e979061. https://doi.org/10.4161/21565562.2014.979061.
52. Phillips, B.T., Williams, J.G., Atchley, D.T., Xu, X., Li, J.-L., Adams, A.L., Johnson, K.L., and Hall, T.M.T. (2019). Mass spectrometric identification of candidate RNA-binding proteins associated with Transition Nuclear Protein mRNA in the mouse testis. Sci. Rep. *9*, 13618. https://doi.org/10.1038/s41598-019-50052-z.
53. Steger, K., Klonisch, T., Gavenis, K., Drabent, B., Doenecke, D., and Bergmann, M. (1998). Expression of mRNA and protein of nucleoproteins during human spermiogenesis. Mol. Hum. Reprod. *4*, 939–945. https://doi.org/10.1093/molehr/4.10.939.
54. Lee, K., Haugen, H.S., Clegg, C.H., and Braun, R.E. (1995). Premature translation of protamine 1 mRNA causes precocious nuclear condensation and arrests spermatid differentiation in mice. Proc. Natl. Acad. Sci. USA *92*, 12451–12455. https://doi.org/10.1073/pnas.92.26.12451.
55. Sutherland, J.M., Sobinoff, A.P., Fraser, B.A., Redgrove, K.A., Siddall, N.A., Koopman, P., Hime, G.R., and McLaughlin, E.A. (2018). RNA binding protein Musashi-2 regulates PIWIL1 and TBX1 in mouse spermatogenesis. J. Cell. Physiol. *233*, 3262–3273. https://doi.org/10.1002/jcp.26168.
56. Braun, R.E. (2000). Temporal control of protein synthesis during spermatogenesis. Int. J. Androl. *23* (*Suppl 2*), 92–94. https://doi.org/10.1046/j.1365-2605.2000.00027.x.
57. Snyder, E., Soundararajan, R., Sharma, M., Dearth, A., Smith, B., and Braun, R.E. (2015). Compound Heterozygosity for Y Box Proteins Causes Sterility Due to Loss of Translational Repression. PLoS Genet. *11*, e1005690. https://doi.org/10.1371/journal.pgen.1005690.
58. Tseden, K., Topaloglu, O., Meinhardt, A., Dev, A., Adham, I., Müller, C., Wolf, S., Böhm, D., Schlüter, G., Engel, W., and Nayernia, K. (2007). Premature translation of transition protein 2 mRNA causes sperm abnormalities and male infertility. Mol. Reprod. Dev. *74*, 273–279. https://doi.org/10.1002/mrd.20570.
59. Park, Y.J., and Pang, M.G. (2021). Mitochondrial Functionality in Male Fertility: From Spermatogenesis to Fertilization. Antioxidants *10*, 98. https://doi.org/10.3390/antiox10010098.
60. Pan, X., Chen, X., Tong, X., Tang, C., and Li, J. (2015). Ppp2ca knockout in mice spermatogenesis. Reproduction *149*, 385–391. https://doi.org/10.1530/rep-14-0231.
61. Du, M., Yuan, L., Zhang, Z., Zhang, C., Zhu, M., Zhang, Z., Li, R., Zhao, X., Liang, H., Li, Y., et al. (2021). PPP2R1B is modulated by ubiquitination and is essential for spermatogenesis. FASEB J. *35*, e21564. https://doi.org/10.1096/fj.202002810R.
62. Roy, A., Lin, Y.N., Agno, J.E., DeMayo, F.J., and Matzuk, M.M. (2007). Absence of tektin 4 causes asthenozoospermia and subfertility in male mice. FASEB J. *21*, 1013–1025. https://doi.org/10.1096/fj.06-7035com.
63. Fiedler, S.E., Dudiki, T., Vijayaraghavan, S., and Carr, D.W. (2013). Loss of R2D2 proteins ROPN1 and ROPN1L causes defects in murine sperm motility, phosphorylation, and fibrous sheath integrity. Biol. Reprod. *88*, 41. https://doi.org/10.1095/biolreprod.112.105262.
64. Xu, K., Yang, L., Zhang, L., and Qi, H. (2020). Lack of AKAP3 disrupts integrity of the subcellular structure and proteome of mouse sperm and causes male sterility. Development *147*. https://doi.org/10.1242/dev.181057.
65. Skerget, S., Rosenow, M.A., Petritis, K., and Karr, T.L. (2015). Sperm Proteome Maturation in the Mouse Epididymis. PLoS One *10*, e0140650. https://doi.org/10.1371/journal.pone.0140650.
66. Ito, C., Akutsu, H., Yao, R., Yoshida, K., Yamatoya, K., Mutoh, T., Makino, T., Aoyama, K., Ishikawa, H., Kunimoto, K., et al. (2019). Odf2 haploinsufficiency causes a new type of decapitated and decaudated spermatozoa, Odf2-DDS, in mice. Sci. Rep. *9*, 14249. https://doi.org/10.1038/s41598-019-50516-2.
67. Yang, K., Grzmil, P., Meinhardt, A., and Hoyer-Fender, S. (2014). Haplo-deficiency of ODF1/HSPB10 in mouse sperm causes relaxation of head-to-tail linkage. Reproduction *148*, 499–506. https://doi.org/10.1530/rep-14-0370.
68. Yamaguchi, R., Muro, Y., Isotani, A., Tokuhiro, K., Takumi, K., Adham, I., Ikawa, M., and Okabe, M. (2009). Disruption of ADAM3 impairs the migration of sperm into oviduct in mouse. Biol. Reprod. *81*, 142–146. https://doi.org/10.1095/biolreprod.108.074021.
69. Yamada, D., Yoshida, M., Williams, Y.N., Fukami, T., Kikuchi, S., Masuda, M., Maruyama, T., Ohta, T., Nakae, D., Maekawa, A., et al. (2006). Disruption of spermatogenic cell adhesion and male infertility in mice lacking TSLC1/IGSF4, an immunoglobulin superfamily cell adhesion molecule. Mol. Cell Biol. *26*, 3610–3624. https://doi.org/10.1128/mcb.26.9.3610-3624.2006.
70. Schneider, C.A., Rasband, W.S., and Eliceiri, K.W. (2012). NIH Image to ImageJ: 25 years of image analysis. Nat. Methods *9*, 671–675. https://doi.org/10.1038/nmeth.2089.
71. Butler, A., Hoffman, P., Smibert, P., Papalexi, E., and Satija, R. (2018). Integrating single-cell transcriptomic data across different conditions, technologies, and species. Nat. Biotechnol. *36*, 411–420. https://doi.org/10.1038/nbt.4096.
72. Yu, G., Wang, L.G., Han, Y., and He, Q.Y. (2012). clusterProfiler: an R package for comparing biological themes among gene clusters. OMICS *16*, 284–287. https://doi.org/10.1089/omi.2011.0118.
73. Korsunsky, I., Millard, N., Fan, J., Slowikowski, K., Zhang, F., Wei, K., Baglaenko, Y., Brenner, M., Loh, P.R., and Raychaudhuri, S. (2019). Fast, sensitive and accurate integration of single-cell data with Harmony. Nat. Methods *16*, 1289–1296. https://doi.org/10.1038/s41592-019-0619-0.

74. Ashburner, M., Ball, C.A., Blake, J.A., Botstein, D., Butler, H., Cherry, J.M., Davis, A.P., Dolinski, K., Dwight, S.S., Eppig, J.T., Harris, M.A., Hill, D.P., Issel-Tarver, L., Kasarskis, A., Lewis, S., Matese, J.C., Richardson, J.E., Ringwald, M., Rubin, G.M., and Sherlock, G. (2000). Gene ontology: tool for the unification of biology. The Gene Ontology Consortium. Nat. Genet. *25*, 25–29. https://doi.org/10.1038/75556.

75. Gene Ontology Consortium (2021). The Gene Ontology resource: enriching a GOld mine. Nucleic Acids Res. *49*. D325–d334. https://doi.org/10.1093/nar/gkaa1113.

76. La Manno, G., Soldatov, R., Zeisel, A., Braun, E., Hochgerner, H., Petukhov, V., Lidschreiber, K., Kastriti, M.E., Lönnerberg, P., Furlan, A., et al. (2018). RNA velocity of single cells. Nature *560*, 494–498. https://doi.org/10.1038/s41586-018-0414-6.

77. Finak, G., McDavid, A., Yajima, M., Deng, J., Gersuk, V., Shalek, A.K., Slichter, C.K., Miller, H.W., McElrath, M.J., Prlic, M., et al. (2015). MAST: a flexible statistical framework for assessing transcriptional changes and characterizing heterogeneity in single-cell RNA sequencing data. Genome Biol. *16*, 278. https://doi.org/10.1186/s13059-015-0844-5.

STAR★METHODS

KEY RESOURCES TABLE

REAGENT or RESOURCE	SOURCE	IDENTIFIER
Antibodies		
Rabbit polyclonal anti-WNK1	Abcam	Cat#ab137687 No RRID
Recombinant rabbit monoclonal anti-WNK1	Abcam	Cat#ab174854 No RRID
Goat polyclonal anti-c-KIT	R and D Systems	Cat# AF1356; RRID: AB_354750
Rat monoclonal anti-GCNA1 (TRA98)	Abcam	Cat# ab82527; RRID: AB_1659152
Alexa Fluor® 647 Mouse monoclonal [Cor 10G11/7] to SCP3	Abcam	Cat#ab205847 No RRID
Goat polyclonal anti-GFP	Abcam	Cat# ab5450; RRID: AB_304897
Rabbit monoclonal anti-phospho-histone H2A.X Ser139	Cell Signaling Technology	Cat# 9718; RRID: AB_2118009
Rabbit monoclonal anti-phospho-4E-BP1 Thr37/46	Cell Signaling Technology	Cat# 2855; RRID: AB_560835
Rabbit monoclonal anti-4E-BP1	Cell Signaling Technology	Cat# 9644; RRID: AB_2097841
Rabbit polyclonal anti-ACRV1	ProteinTech	Cat# 14040-1-AP; RRID: AB_10640426
Rabbit anti-ACRBP	ThermoFisher Scientific	Cat# PA5-58649; RRID: AB_2637614
Rabbit anti-SPESP1	ThermoFisher Scientific	Cat# PA5-62301; RRID: AB_2647845
Mouse anti-Beta-Actin	Sigma-Aldrich	Cat# A5441; RRID: AB_476744
Rabbit anti-mTOR	Cell Signaling Technology	Cat# 2983; RRID: AB_2105622
Rabbit anti phospho-mTOR	Cell Signaling Technology	Cat# 2971; RRID: AB_330970
Chemicals, peptides, and recombinant proteins		
RA	Millipore Sigma	R2625
WIN 18,446/BDAD	Caymenchem	14018
TAM	Millipore Sigma	T5648
Critical commercial assays		
In situ Cell Death Detection Kit	Roche	1684795910
BCA Kit	Pierce	23225
Deposited data		
Raw and analyzed data	This paper	GEO: GSE234068
Experimental models: Organisms/strains		
Mouse: *Wnk1*$^{f/f}$: B6.129-Wnk1<tm1Clhu>	The Huang Laboratory	MGI:4360972
Mouse: *Wnk1*$^{f/f}$*; Wnt7a-Cre*: B6.Cg-Wnk1<tm1Clhu> Tg(Wnt7a-EGFP/cre)Bhr	This study	NA
Mouse: *mT/mG;Wnt7a-Cre*: B6.Cg-Gt(ROSA)26Sor<tm4(ACTB-tdTomato,-EGFP)Luo> Tg(Wnt7a-EGFP/cre)Bhr	This study	NA
Mouse: *Sun1*^{GFP}*;Wnt7a-Cre*: B6.Cg-Gt(ROSA)26Sor<tm5(CAG-Sun1/sfGFP)Nat> Tg(Wnt7a-EGFP/cre)Bhr	This study	NA
Mouse: *Wnk1*$^{f/f}$*; Hspa2*-Cre: B6.129-Wnk1<tm1Clhu> Tg(Hspa2-cre)1Eddy	This study	NA
Mouse: *Wnk1*$^{f/f}$*; Ddx4-Cre*^{ERT2}:Wnk1<tm1Clhu> Tg(Ddx4-cre/ERT2)1Dcas	This study	NA
Software and algorithms		
GraphPad, Prism Software	Dotmatics	N/A

(*Continued on next page*)

Continued

REAGENT or RESOURCE	SOURCE	IDENTIFIER
ZEN	Zeiss	https://www.zeiss.com/microscopy/en/products/software/zeiss-zen.html
ImageJ/FIJI	Schneider et al.[70]	https://ImageJ.nih.gov/ij/
QIAGEN Ingenuity Pathway Analysis (IPA) software	Krämer et al.[39]	https://digitalinsights.qiagen.com/products-overview/discovery-insights-portfolio/analysis-and-visualization/qiagen-ipa/
GSEA	Subramanian et al.[41] and Mootha et al.[40]	https://www.gsea-msigdb.org/gsea/index.jsp
R (version 4.0.2)	GNU project	www.r-project.org
Cell Ranger Single-Cell Software Suite (version 6.0.1)	10X Genomics Inc., CA	https://support.10xgenomics.com/single-cell-gene-expression/software/overview/welcome
Seurat R package (version 4.0.2)	Butler et al.[71]	https://satijalab.org/seurat/
DecountX (R package celda, Version 1.4.7)	Bioconductor	https://github.com/campbio/celda
R package ClusterProfile (V3.18.1)	Yu et al.[72]	https://github.com/YuLab-SMU/clusterProfiler
R package "harmony" (Version 1.0.0)	Korsunsky et al.[73]	https://github.com/immunogenomics/harmony
Monocle3 (Version 1.0.0)	Qiu et al.[34]	https://cole-trapnell-lab.github.io/monocle3/
GO annotation of Biological Processes	Ashburner et al.[74] Gene Ontology Consortium[75]	http://geneontology.org/
python package *velocyto.py* (Version 0.17)	La Manno et al.[76]	https://velocyto.org/velocyto.py/index.html

RESOURCE AVAILABILITY

Lead contact

Further information and requests for resources and reagents should be directed to and will be fulfilled by the lead contact, Francesco DeMayo (francesco.demayo@nih.gov).

Materials availability

This study did not generate new unique reagents.

Data and code availability

- All the sequencing data are publicly available as of the date of publication and has been deposited at the Gene Expression Omnibus (GEO) with the accession number GEO: GSE234068 also listed in the key resources table.
- This paper does not report original code.
- Original western-blot images,IF and microscopy pictures reported in this paper and any additional information required to reanalyze the data reported in this paper are available from the lead contact upon request.

EXPERIMENTAL MODEL AND STUDY PARTICIPANT DETAILS

The mice used in this study were: *Wnk1*$^{f/f}$ (B6.129-Wnk1<tm1Clhu>), *Wnk1*$^{f/f}$; *Wnt7a-Cre* (B6.Cg-Wnk1<tm1Clhu> Tg(Wnt7a-EGFP/cre)Bhr), *mT/mG*;*Wnt7a-Cre* (B6.Cg-Gt(ROSA)26Sor<tm4(ACTB-tdTomato,-EGFP)Luo> Tg(Wnt7a-EGFP/cre)Bhr), *Sun1*^{GFP};*Wnt7a-Cre* (B6.Cg-Gt(ROSA)26Sor<tm5(CAG-Sun1/sfGFP)Nat> Tg(Wnt7a-EGFP/cre)Bhr), *Wnk1*$^{f/f}$; *Hspa2-Cre* (B6.129-Wnk1<tm1Clhu> Tg(Hspa2-cre)1Eddy), *Wnk1*$^{f/f}$; *Ddx4-Cre*^{ERT2} (Wnk1<tm1Clhu> Tg(Ddx4-cre/ERT2)1Dcas), CD-1 and wildtype C57BL/6J mice. All experimental mice were male. The mice were kept at the animal facility of the National Institute of Environmental Health Sciences under barrier conditions and at 12-h light and 12-h dark cycles. The animal facility is maintained at 20.5 ^{o}C – 23.9 ^{o}C and 50% $\pm$ 15% humidity, with free access to food and water. For spermatogonial synchronization, postnatal CD-1 mice were used. For phenotype characterization, post-pubertal mice between the age of 6 and 8 weeks were used at the start of the experiment. For the scRNA-seq, six- and seven-week-old mice were used. Genotypes were determined by conventional PCR using isolated DNA from tails, and was performed by Transnetyx. All animal studies were conducted in accordance with the Guide for the Care and Use of Laboratory Animals published by the National Institute of Health and animal protocols were approved by the Institutional Animal Care and Use Committee at the National Institute of Environmental Health Sciences.

METHOD DETAILS

Spermatogonial synchronization

Starting at postnatal day 1 (P1), wildtype CD-1 pups (Charles River Laboratories) were fed daily with 100 μg of WIN 18,446 (BDAD, 14018, Caymenchem) per gram body mass. Briefly, Kimwipe-lined pipette boxes are prewarmed on slide heater set to 40°C, and working BDAD solution (prepared to 100 mM in DMSO) were equilibrated to 37°C. Pups were placed in the pre-warmed pipette box, and weighed to determine BDAD dosage. The feeding needles were prepared by removing ~ 2 cm from the narrow end of an unfiltered P200 tip, followed by inserting the cut-side of the pipette tip into a 24-gauge reusable feeding needle. The assembly was mounted onto a P20 pipette. The appropriate volume of BDAD solution was drawn using the prepared feeding needle, and inserted into the pup's mouth, followed by depressing the pipette to eject the solution. This was done incrementally, dispensing 2–3 μL at a time. The pups were then placed back into prewarmed pipette box, and closely monitored for at least 10 min before returning to the cage. On P11, the pups were administered with 10 μg/g RA subcutaneously (R2625, Millipore Sigma). RA was prepared in DMSO to a working concentration of 5 μg/μL and stored at −20°C, and subcutaneous administration was achieved using 1 cc syringe and 30-gauge needle. The pups were returned to the cage, and euthanized at the appropriate time points to obtain testes with germ cells at the desired stage of spermatogenesis: P14 = A_3 differentiated spermatogonia, P17 = B spermatogonia, P19 = preleptotene spermatocytes, P20 = leptotene spermatocytes, P23 = early stage pachytene spermatocytes, and P26 = mid-stage pachytene spermatocytes.

Tamoxifen (TAM) treatment

To induce CRE activity in the *Wnk1*$^{f/f}$; *Ddx4-Cre*^{ERT2} mice, post-pubertal *Wnk1*$^{f/f}$ (control) and *Wnk1*$^{f/f}$; *Ddx4-Cre*^{ERT2} (*Wnk1* knock-out) mice were subjected to TAM treatment. Powder form TAM (T5648, Millipore Sigma) was prepared to a concentration of 20 mg/mL or 40 mg/mL in corn oil (C8267, Millipore Sigma), aliquoted and stored at −20°C. For treatment, aliquots were thawed to room temperature (RT), and administered via intraperitoneal injection using a 26-gauge needle at 1 mg per 10g body mass for five consecutive days. The mice were kept for at least five weeks to complete one cycle of spermatogenesis before conducting downstream experiments, including fertility trial or tissue collection for protein expression analyses.

Fertility trial

Post-pubertal *Wnk1*$^{f/f}$ and *Wnk1*$^{f/f}$; *Wnt7a-Cre* mice were housed with 6-week-old wildtype C57BL/6J female mice (The Jackson Laboratory) for a period of 6 months. The mice were monitored daily for pregnancy and delivery. Upon the first observation of delivery, the total number of pups was documented.

Tissue processing for histology, immunohistochemistry and immunofluorescence

After euthanization, the testes and epididymides were collected and washed in PBS, followed by 24 to 48-h fixation in 4% paraformaldehyde (28908, ThermoFisher Scientific) diluted in PBS at 4°C with shaking. Tissues were then placed in 70% ethanol for a minimum of 48 h, followed by dehydration, paraffin embedding and sectioning to 5 μm thickness. Sections were deparaffinized by 3 serial incubations in Citrisolv clearing agent (22-143-975, ThermoFisher Scientific) and rehydrated through decreasing ethanol dilutions.

Histology

Sections were subjected to hematoxylin staining for 1–5 min, then destained in acidic alcohol for a few seconds. After several washes in tap water, tissues were blued in saturated lithium carbonate. and eosin staining, followed by dehydration through increasing ethanol dilutions, with incubation in Citrisolv before mounting.

Immunohistochemistry

Sections were subjected to antigen retrieval after rehydration using the VECTOR Laboratories Antigen Unmasking Solution as per manufacturer's instructions (H-3300). Blocking of endogenous peroxidase was performed by treating the sections with 3% H_2O_2 for 10 min at RT. Tissues were blocked in 5% normal donkey serum (NDS) or normal goat serum for 60 min at RT, then incubated with primary antibody at 4°C overnight. The slides were washed twice in PBS, and secondary antibody diluted in 1% w/v bovine serum albumin (BSA) was applied. The ABC reagent was applied to tissue according to the manufacturer's instructions (PK-6100, VECTOR Laboratories). Signals were developed using the VECTOR Laboratories DAB ImmPACT Staining Kit. Finally, the tissue sections were counterstained with hematoxylin and dehydrated through increasing ethanol concentration, followed by Citrisolv incubation and mounting using Permount (SP15-100, ThermoFisher Scientific).

If from paraffin embedded tissues

Tissue sections were prepared and subjected to antigen retrieval as described above, then blocked in 0.4% v/v Triton X-100, 1% BSA, and 5% NDS for 60 min followed by overnight incubation in primary antibody prepared in 0.4% Triton X-100/PBS at 4°C. Sections were washed in PBS and incubated with secondary antibodies diluted in 0.4% Triton X-100/PBS for 90 min. Finally, slides were washed 3 times in PBS and coverslipped in DAPI-containing mounting medium (H-1400 or H-1800, Vector Laboratories).

If from cryopreserved sections

After mice euthanization, the testes were washed in PBS and incubated in 4% paraformaldehyde overnight, followed by five 1-h washes in PBS with shaking at 4°C. Testes were then incubated in 30% w/v sucrose prepared in PBS at 4°C until it sank. Testes are embedded in Tissue-Tek O.C.T. Compound (4583, Sakura), and frozen at −80°C for at least 2 h. Tissue blocks were then sectioned on a cryotome (Leica) to 5 μm thickness and stored at −20°C or −80°C until ready for staining. Sections were briefly hydrated in PBS for 5 min, followed by permeabilization in 0.1% v/v Triton X-100/PBS for 5 min. Sections were then blocked in 3% w/v BSA in PBS with 0.1% v/v Triton X-100 for 1 h at RT, followed by incubation with primary antibody (prepared in blocking buffer) for 1 h at RT. After three washes in PBS, the sections were incubated with secondary antibodies in blocking buffer for 1 h at RT. After three final PBS washes, the slides were mounted in DAPI containing mounting medium (H-1400 or H-1800, Vector Laboratories).

Confocal microscopy

All fluorescence images shown were captured using the Zeiss LSM 780 UV confocal microscope. Tissue sections were scanned by collecting z stack images at 2 μm intervals, followed by maximum intensity projection processing.

TUNEL assay

Cell death was assessed in the control and *Wnk1*$^{f/f}$*; Wnt7a-Cre* testes using the *In situ* Cell Death Detection Kit (#11684795910, Roche) according to the manufacturer's instructions. Briefly, formalin fixed paraffin embedded tissues were first sectioned to 5 μm, then deparaffinized in Citrisolv and hydrated through decreased ethanol % (100% X 3, followed by 95%, then 70%, then water). Sections were treated with 20 μg/mL proteinase K (25530-049, Invitrogen) prepared in 10 mM Tris-HCl for 30 min at 37°C. After a brief PBS wash, the sections were incubated with TUNEL reaction mixture (50 μL of enzyme solution mixed into 450 μL Label solution just prior to use) for 60 min at 37°C. Sections were washed 3 X in PBS, followed by coverlipping in DAPI containing mounting medium (H-1800, Vector Laboratories). Note that for each experiment, a negative and positive control were included. For the positive control, the tissue section was incubated with 0.05 U/μL DNase I (18068-015, Invitrogen) for 10 min at RT to artificially induce DNA damage prior to labeling with the TUNEL reaction mixture. For the negative control, the section was incubated with only the Label solution (without the enzyme).

Protein extraction

Whole testes were homogenized in RIPA Lysis and Extraction Buffer (89900, ThermoFisher Scientific) supplemented with protease inhibitor cocktail (11836170001, Roche Diagnostics) and phosphatase inhibitor cocktail (4906837001, Roche Diagnostics), then centrifuged at 10,000 G for 10 min at 4°C. The supernatant containing the protein were measured using the BCA Kit (23225, Pierce, ThermoFisher Scientific) and stored at −80°C until ready for analysis.

Western blotting

Heat-denatured protein samples were resolved using 7.5%, 10%, or gradient 4%–20% Criterion Tris-HCl precast gels (Bio-Rad), followed by transferring using the Trans-Blot Turbo Transfer System (Bio-Rad), as per the manufacturer's instructions. PVDF and nitrocellulose membranes were used for target proteins more than 200 kDa and less than 200 kDa, respectively. After transfer, the membranes were blocked in 5% w/v nonfat milk or BSA. Membranes were incubated with primary antibody at 4°C overnight, washed 3 times, and incubated in secondary antibody the next day. Finally, membranes were washed another 3 times, and signal was detected using peroxidase chemiluminescent substrates (Clarity Western ECL Substrate 1705060 from Bio-Rad or Amersham ECL Prime Western Blotting Detection Reagent RPN2232 from GE Healthcare Life Sciences). GAPDH or β-tubulin were detected as the loading control.

Single-cell RNA-sequencing

In total, three *Wnk1*$^{f/f}$ and two *Wnk1*$^{f/f}$*; Wnt7a-Cre* adult mice between six and eight weeks of age were used in two independent sequencing experiments. After euthanization, testes were collected in HBSS (14025092, ThermoFisher Scientific) and the tunicas were removed. The tubules were then placed into 0.25% Trypsin with 0.7 mg/mL DNaseI, and incubated at 37^{O}C for 5 min, after which an additional 1 mL of 7 mg/mL DNaseI were added, and incubation repeated. A final 1 mL of 7 mg/mL DNaseI was added, and tubules were gently pipetted up and down to disperse any remaining clumps. The trypsin was neutralized with 1 mL of FBS, and filtered through a 40 μm cell strainer, and pelleted with centrifugation at 600 G for 7 min at 4^{O}C. For library preparation and sequencing, the single-cell suspension from each sample were counted and examined for viability using an auto cell counter (Bio-Rad TC20). Approximately 6000 live cells from each sample at a concentration of $<5\times10^5$ cells/mL were loaded into the Single Cell Chip followed by forming single cell emulsion in Chromium Single Cell Controller (10x Genomics, Chromium Single Cell 3′ Library & Gel Bead Kit). The mRNA reverse transcription, cDNA generation and amplification, and single cell gene expression library construction were carried out according to the protocols provided by the manufacture. The libraries were then sequenced by the NIEHS Epigenomics and DNA Sequencing Core Laboratory on NextSeq 500 and NovaSeq 6000 (Illumina) with paired-end sequencing (Read 1: 30; Read 2: 100). At least 60,000 reads/cell were obtained for all four samples.

QUANTIFICATION AND STATISTICAL ANALYSIS

Single-cell RNA-sequencing data processing

Raw read processing was carried out using the Cell Ranger Single-Cell Software Suite (version 6.0.1, 10X Genomics Inc., CA). Briefly, the demultiplexed FASTQ files (paired-end, Read 1: 30 bp, Read 2: 100 bp) were generated using the CellRanger *mkfastq* command. Primary data analyses to determine gene transcript counts per cell were done (including alignment, filtering, barcode counting and UMI quantification); quality control, and statistical analysis were performed using CellRanger *count* command. Gene positions were annotated using Ensembl build 98.

Gene expression quantification and filtering

Raw gene expression matrices generated per sample using the CellRanger Software (version 6.0.1) were imported into R (version 4.0.2) and converted to a Seurat object using the Seurat R package (version 4.0.2).[71] The ambient RNA was cleaned using DecountX (R package celda, Version 1.4.7). Dead cells and doublets were removed. The total number of UMIs and genes, and the UMIs derived from mitochondrial genome were counted. Cells which had over 15% mitochondria-derived UMIs were discarded. Then, the upper bound was calculated as mean plus two standard deviation (SD) and the lower bound as mean minus two SD for both the total UMIs and genes, respectively. Finally, cells with total UMIs or genes outside of the upper and lower bounds were removed.

Data integration and determination of the major cell types

The remaining 19269 out of 26093 cells from the four samples were integrated together and batch effects were corrected using reciprocal PCA ('RPCA') from Seurat R package. First, gene expression matrices were normalized to total cellular read count and Cell-Cycle scores were calculated using Seurat *CellCycleScoring* function for each sample. Then, Seurat *SCTransform* function was applied for the normalized data to remove cell cycle effect and select highly variable genes (HVGs). We selected 2,000 common HVGs from four HVG list using *SelectIntegrationFeatures* and calculated PCA for each samples data based on new HVG genes. Then, all cells from the four samples were integrated using the function *FindIntegrationAnchors* with parameter "reduction = "rpca", normalization.method = "SCT" and function *IntegrateData*. We checked HVG and removed mitochondrial genes. Following that, PCA for cleaned HVGs were rescaled and re-calculated. The *RunUMAP* function was then applied to conduct the Uniform Manifold Approximation and Projection (UMAP) dimensional reduction. The *FindNeighbors* constructed a Shared Nearest Neighbor Graph, and *FindClusters* function with "resolution = 0.6" parameter was carried out to cluster cells into different groups. The canonical marker genes were applied to annotated cell clusters to known biological cell types.

Identification of marker genes and differential expression genes (Differentially expressed genes)

To identify marker genes for these cell types, we compared the gene expression values of cells from the cluster of interest to that of cells from all other clusters using the Seurat *FindMarkers* function with default parameter of "MAST" test.[77] Marker genes were defined based on the following three criteria: 1) the average expression value in the cluster of interest was at least 1.2-fold higher than the average expression in the rest of clusters; 2) were detectable in greater than 10% of the cells in the cluster of interest; and 3) exhibit the highest mean expression in the cluster of interest compared to all other clusters. To calculate the DEGs between two groups of cells, e.g., *Wnk1*$^{f/f}$*; Wnt7a-Cre* vs. *Wnk1*$^{f/f}$ Seurat *FindMarkers* function with method "MAST" were applied for two groups of cells with parameter "min.pct = 0.01, logfc.threshold = 0.01". For marker genes and DEG lists, GO and pathway analyses were performed by R package ClusterProfile (V3.18.1).[72]

Sub-cell type analysis

Raw gene expression count of cells for sub-cell type were extracted from previous cleaned data and merged to a Seurat object using the Seurat. Gene expression matrices were normalized to total cellular read count, and HVGs selected from the normalized data using Seurat *SCTransform* function with default parameters. Batch effects were observed and corrected using R package "harmony" (Version 1.0.0).[73] The same procedures as described for whole cell population were then used for dimensional reduction and clustering.

Trajectory and RNA velocity analysis

Trajectory and pseudotime analysis were conducted by monocle3 (Version 1.0.0).[34] For RNA velocity analysis, gene-relative velocity was estimated by python package *velocyto.py* (Version 0.17).[76] To keep the data analysis consistent, cell coordinates of UMAP generated by Seurat were passed to *monocle* and *velocyto.R*.

Gene ontology analysys

The ontology enrichment analysis was done using the TopGO R package (https://doi.org/10.18129/B9.bioc.topGO). The gene universe consisted of all expressed genes captured in the scRNA-seq (Table S1), while the genes of interested were those categorized as DEGs based on the following criteria: adjusted p value <0.05, base mean >0.2, and Log (2) fold-change >0.2 or < −0.2. The corresponding TopGOdata object was built using "annFUN.org" for the Biological Processes gene ontology annotation.[74,75] To run the enrichment analysis, the function runTest was used with a classic algorithm considering each gene ontology category independently, and a Fisher's exact test for statistical enrichment. The full list of significant terms is shown in Table S4.

Quantification analysis

The FIJI/ImageJ software was used for all image-based quantifications.[70] For the round spermatids (Figure 3E), the spermatocytes and elongating spermatids were manually excluded based on SYCP3 (spermatocytes) and DAPI morphology (elongating spermatids) using the 'clear' or 'clear outside' functions. The processed image containing the round spermatids (as indicated by DAPI signal) were subjected to Gaussian blur and Threshold processing, followed by using 'analyze particle' function to count the number of spermatids. The number of round spermatids was then normalized to the length of the tubule. Each dot in Figure 3E represents one tubule, and 15 tubules from three independent mice between stages I – VIII were counted for each genotype. Line indicates median, and ****$p < 0.0001$ based on the Mann-Whitney U test. For quantification of the meiotic spermatocytes (Figure 3G), we first staged the tubules and categorized the spermatocytes into leptotene (stages IX – X), zygotene (stage XI – XII), early pachytene (stages I – VI), mid-pachytene (stages VII – VIII), late-pachytene (stages IX – X), and diplotene (stage XI). SYCP3 signal was used to guide the selection of cells of interest. In stage VIII – XII tubules where there are two populations of SYCP3-positive cells, the 'clear' or 'clear outside' function was used to isolate the target cells. The target cell population was subjected to Gaussian blue and Threshold processing, followed by mask creation which outlines the SYCP3 signal. The 'binary-watershed' function was then used to separate joined cells, and the cell number were then counted using 'analyze particle', where size selection of 35-infinity was used to exclude other smaller, non-specific signal. Results shown are mean $\pm$ SD (n = 5 tubules from 2 mice), *$p < 0.05$ based on two-tailed Student's *t* test. For quantification of apoptotic cells (Figure 3I), we used the same method as for quantifying the round spermatids, except instead of using DAPI signal, we used TUNEL signal to guide the counting. Each dot in Figure 3I represents one tubule and lines indicate median, and a total of 128 and 215 tubules were counted for each genotype from 3 independent mice (6 mice in total). ****$p < 0.0001$ based on the Mann-Whitney U test. For quantification of phosphorylated and total EIF4EBP1 signal (Figure 5G), we first staged tubules to ensure that we quantify pachytene spermatocytes in mid-to late-stage pachynema where *Wnt7a-Cre* expression was detected. Using SYCP3 signal to guide the selection of pachytene spermatocytes, the population of interest was isolated using the 'clear' and 'clear outside' function. Then, using the Gaussian blur and Threshold function, the phosphorylated or total EIF4EBP1 signal was processed from the spermatocyte population of interest. A mask was then created which outlines the cytoplasmic regions of the cells of interest. The mask is applied to the original, unedited image, and signal intensity was then measured within the selected regions. Results shown are mean $\pm$ SD (n = 6 tubules from 3 independent mice), **$p < 0.001$ based on two-tailed Student's *t* test.